INNOVATIONS IN MODELING CRYOGENIC PROPELLANT PHASE CHANGE

FOR LONG DURATION SPACEFLIGHT

A Dissertation

Submitted to the Faculty

of

Purdue University

by

Praveen Srikanth

In Partial Fulfillment of the

Requirements for the Degree

of

Doctor of Philosophy

December 2019

Purdue University

West Lafayette, Indiana

THE PURDUE UNIVERSITY GRADUATE SCHOOL
STATEMENT OF DISSERTATION APPROVAL

Dr. Steven H. Collicott, Chair

      School of Aeronautics and Astronautics

Dr. Stephen D. Heister

      School of Aeronautics and Astronautics

Dr. Timothee L. Pourpoint

      School of Aeronautics and Astronautics

Dr. Haifeng Wang

      School of Aeronautics and Astronautics

Approved by:

      Dr. Gregory A. Blaisdell

          Head of the School Graduate Program

ACKNOWLEDGMENTS

TABLE OF CONTENTS

LIST OF TABLES

LIST OF FIGURES

NOMENCLATURE

α	Accommodation Coefficient
$\dot{m}$	Mass Flux
μ	Viscosity
ρ	Density
C_p	Specific Heat
F_v	Additional Forces
g	Acceleration Due to Gravity
k	Thermal Conductivity
L_b	Enthalpy of Vaporization
M_v	Molecular Mass of Vapor
P	Pressure
R	Universal Gas Constant
T	Temperature
t	Time
v	Velocity
E	Energy
q	Heat Flux
Π	Disjoining Pressure
σ	Surface Tension
κ	Interface Curvature

Subscripts

l	Liquid
v	Vapor
i	Interface

ABSTRACT

Srikanth, Praveen Ph.D., Purdue University, December 2019. Innovations in Modeling Cryogenic Propellant Phase Change for Long Duration Spaceflight. Major Professor: Steven H. Collicott.

Cryogenic propellants are going to be the cornerstone for effective future human space exploration. These propellants need to be stored and maintained at really low temperatures for a long duration. Accurate phase change modeling is necessary for characterizing the thermal state of future cryogenic propellant tanks and for designing systems to alleviate the self pressurization problem. Better understanding about how to properly store and manage cryogenic propellants would help greatly with In-Situ Resource Utilization (ISRU) strategies for future missions to Mars and further. Predicting the fluid flow, heat transfer, and phase change mass transfer in long term cryogenic storage using CFD models is greatly affected by our understanding of the accommodation coefficient. The kinetically limited phase change model governed by the Hertz-Knudsen-Schrage equation is the model of choice for such calculations. The value of the accommodation coefficient required for the model is unknown for cryogenic propellants. Even in the case of water, the value of the accommodation coefficient has been found to vary over three orders of magnitude based on 80 years of measurements. Experiments specifically built to study accommodation coefficient are needed to estimate the value of the accommodation coefficient and understand some of the uncertainties surrounding these models.

Two phase change models, viz. the thermally limited and the kinetically limited phase change model are implemented in OpenFOAM. Different approaches to implement the Hertz-Knudsen-Schrage equation in a sharp interface conjugate heat transfer solver are studied. Evaporation and condensation calculations for a liquid hydrogen meniscus inside an aluminum container are compared with experimental measure-

ments. The effect of accommodation coefficient on phase change is then studied with the kinetically limited model by comparing with the thermally limited model and the experimental measurements. The uncertainties associated with the temperature and pressure measurements in the experiment are quantified to show their effect on computational predictions. Since cryogenic propellants are perfectly wetting fluids, modeling the thin-film region close to the contact line leads to a multi-scale computational problem. However, the phase change contribution from the thin-film region is approximated in these computations to show the importance of modeling the contact line region accurately to adequately capture the small local thermodynamics in that region.

1. INTRODUCTION & LITERATURE REVIEW

With the ongoing emphasis on human space exploration beyond low earth orbit, the ability of deep space cryogenic propellant storage and refueling is critical in determining the scale of these missions. SpaceX with their interplanetary transport system using the Big Falcon Rocket (BFR) propose to have in-orbit refueling for their spacecrafts using propellant tankers launched from the earth's surface. This would ensure that there is enough propellant to make the trip to the moon and back. But for longer missions such as to Mars, there is still a need for additional refueling on the surface of Mars to make the journey back. Refueling in space also reduces the propellant and inert masses (from systems required to maintain propellants at optimum conditions) at launch, which can then be made available for additional payload on these missions. Thus, it is quite evident that there is a need to improve our understanding of existing technologies and develop new ones for long duration storage and transfer of these propellants in order to achieve our long term goals in space exploration.

Chemical propulsion seems to be the most viable propulsion technology available to us for long term planning of space missions and cryogenic propellants are very lucrative due to their high specific impulse and efficiency. The biggest problem with cryogenic propellants is storing them over long durations due to the self pressurization of the propellant tanks. Despite best efforts to minimize heat leaks by adequately insulating the propellant tanks, there is always some small amount of heat leak into the system. This causes the propellant to boil off and the tank to subsequently self pressurize. The longest that cryogens have been stored and used in flight is 9 hours on the Titan Centaur 5 mission [1]. Self pressurization and pressure control of propellant tanks have been identified as some of the core interests in alleviating some of the problems associated with long term cryogenic storage [2,3]. Traditionally, this excess pressure is managed by venting some vapor from the ullage with the help of thrusters.

Although this would help with the self pressurization problem, it is estimated to cause about a 3% loss of propellant every month [4]. Such a system might work well for on surface applications and over short duration but over longer periods of time the added propellant mass needed to sustain such a system as well as designing a system robust and reliable to withstand the large number of venting cycles would quickly make this impractical and expensive. Other considerations such as the orientation of the ullage in zero gravity also need to be evaluated while designing systems for venting vapor. If not accounted for and managed properly, there is always a chance that we could be venting a two phase fluid which would need additional care. Venting propellants may also pose safety risks in the vicinity of these storage tanks which is an important consideration for crewed flight missions.

There is potential for ventless pressure control systems to manage self pressurization in these propellant tanks. Experiments such as the Zero Boil Off Tank (ZBOT) [5,6] experiment aboard the International Space Station and the Tank Pressure Control Experiment (TPCE) [7] flown during the shuttle era help advance the technology for such ventless pressure control systems. Such active pressure control systems usually use a combination of active cooling techniques like spray bars and fluid mixing jets to control the ullage pressure and generally require continuous power to function. There have been numerous studies to characterize tank self pressurization mainly to estimate the amount of pressure rise anticipated and to look at the various mechanisms which contribute to this pressure rise. In 1967, Aydelott [8,9] examined tank self-pressurization under 1-g and reduced gravity conditions using a $9\,in.$ spherical liquid hydrogen tank. It was found that the rate of pressure rise was lower in reduced gravity conditions due to an increase in wall wetted surface area and an increase in boiling. It was also found that the rate of pressure rise was mostly affected by the heater configuration and not so much by the liquid fill level. To further study the effect of tank sizing on self-pressurization, Aydelott and Spuckler [10] conducted similar experiments with a ventless $22\,in.$ spherical liquid hydrogen tank.

They showed that the pressure rise should be near identical in two uniformly heated tanks for equal values of heat added per unit volume.

Hasan et al. [11] experimentally investigated self pressurization and thermal stratification in a flight weight LH2 tank which was subjected to low heat fluxes ranging from $0.35\,W/m^2$ to $3.5\,W/m^2$. They found that the pressure rise rate and thermal stratification increased with increase in heat flux. It was also found that the initial transient pressure rise was dependent on the initial condition from which the tank was allowed to pressurize. The effect of fill level in such a tank was experimentally verified in a 1-g environment by Lin, Hasan, and Van Dresar [12]. They evaluated pressure rise at fill levels of 29%, 49%, and 83% and found that for an oblate spheroidal tank geometry, the lowest rate of pressure rise for LH2 was in the case of the 49% fill level.

There have also been studies to evaluate different techniques to control this self pressurization by using active pressure control mechanisms such as mixing jets and spray bars. Poth and Van Hook [13] showed that tank pressurization could be reduced under reduced gravity by using mixing jets as they help reduce thermal stratification in the tank. This was further investigated by Lin, Hasan, and Van Dresar [14] experimentally using large storage tanks. They observed that the change in tank pressure was affected by subcooled jet mixing as well as the convection boundary layer formed from wall heating. The use of a spray bar TVS to thermally de-stratify the tank, thereby controlling the self pressurization, was demonstrated using the Multi Hydrogen Test Bed (MHTB) LH2 Tank at Marshall Space Flight Center [15]. With such a set up they were able to maintain the ullage pressure within a $\pm 3.45\,kPa$ control band. Zero gravity tank pressurization and pressure control data is mainly available from three experiments, viz., the Saturn AS-203 experiment [16], the Tank Pressure Control Experiment (TPCE) [7], and the Zero Boil Off Tank Experiment (ZBOT) [5]. The Saturn AS-203 experiment is one of the earliest low gravity cryogenic self pressurization tests and reported a mean pressure rise rate of $17\,psi/hr$ in the case of a closed LH2 tank. TPCE flew on board the space shuttle on STS-52 and used jet induced mixing in a partially filled tank with simulant fluid to study tank pressure

control. They also concluded that the interaction of the mixing jet with the ullage can be classified based on the jet Weber number and that at higher Weber numbers the jet completely penetrated the ullage. More recently, a series of three experiments called the Zero Boil Off Tank Experiments [5] have been proposed to be flown to the International Space Station to gather data related to tank pressurization and pressure control mechanisms. These experiments use a simulant fluid and look at the thermal stratification, self pressurization, and pressure control using mixing jets (ZBOT-1, 2017), spray bars, and other active pressure control mechanisms (ZBOT-3). ZBOT-2 proposed to fly in 2022 is expected to study the effect of non-condensable gases on evaporation and condensation rates during pressurization and pressure control phases. A preliminary 1-g experiment was previously conducted [17] to study the feasibility of such microgravity tank experiments and to help with design decisions for the ISS experiments.

However, conducting such full scale experiments to get sufficient microgravity data and characterize such propellant storage systems would be very expensive and impractical in the long run due to the large range of size and time scales involved. Reliable CFD modeling for these systems would aid mission design by better determining the thermal state of these cryogenic storage tanks, as propellant boil off is often a limiting factor and zero boil-off requires continuous power. This dissertation focuses on addressing some of the uncertainties associated with phase change modeling for predicting tank pressurization and pressure control systems. This would help advance the field to a point where differences in measurements are understood and would enable dependable CFD modeling in the future for cryogenic storage systems.

This dissertation consists of six chapters including this current chapter. The second chapter consists of a literature survey of existing studies pertaining to accommodation coefficients and modeling tank self pressurization. The different phase change models available and their implementation in OpenFOAM are also detailed in this chapter. Chapter 3 describes a benchmark case setup to draw comparisons between the different implementations of the phase change models to help understand

some of the trends observed. Chapter 4 outlines a test case based on the LH2 phase change experiment conducted by Bellur et al. [18] at the National Institute of Standards and Technology (NIST). Experimental data from this study is used to draw comparisons with computational predictions to look at the effect of accommodation coefficient on evaporation rate predictions. Chapter 5 addresses some of the uncertainties inherent in the experimental measurements and presents data to evaluate the effect of these uncertainties on evaporation rate predictions. Chapter 6 summarizes the results presented and makes recommendations for future experiments designed to study accommodation coefficients for similar fluid systems.

2. NUMERICAL APPROACH

To design tanks for cryogenic storage efficiently in the future, there is a need to use computational methods to evaluate new tank designs and establish the thermal state of these tanks in reduced gravity conditions. With this as the focus, the use of theoretical and computational methods to predict phase change in cryogenic fluids and self pressurization in cryogenic storage systems has been the thesis of quite a few studies recently. Lin and Hasan [19] conducted a theoretical study to look at the effect of tank sizing, liquid fill level, and wall heat flux in microgravity conditions on spherical LH2 tanks. They found that the tank pressure initially increases faster for higher fill levels because of the effect of liquid thermal expansion, but later due to interface evaporation the pressure increase was faster for lower fill levels. Hochstein et al. [20] used an in-house computational solver to show the viability of coupling an axial mixing jet with a traditional thermodynamic vent system to effectively control tank pressurization. Hochstein et al. [21] then used an effective conductivity model to account for some convection in normal and reduced gravity conditions which would be normally neglected if a pure conduction model is assumed for the liquid phase. The vapor was assumed to be in a quasi-static thermal equilibrium state and tank self pressurization was computed in liquid hydrogen tank systems. In their study they found good agreement between the computationally predicted rate and available experimental data for both scale sized and full sized liquid hydrogen tanks. The effect of initial sub cooling as well as the tank fill level on self pressurization were studied with this model.

To demonstrate the use of CFD to study tank pressurization, Grayson et al. [22] used the FLOW-3D code to model the AS-203 tank experiment aboard the Saturn S-IVB rocket and computed tank self pressurization as well as thermal stratification with reasonable accuracy. In comparison to the experimental data, they found a

3.5% deviation in average ullage pressurization rate and a 6% difference in the ullage temperature rise rate. Panzarella and Kassemi [23] used a code which coupled a lumped thermodynamic model for the vapor phase with the full Navier Stokes and energy equations for the liquid phase to compute tank pressurization for three different heating configurations viz. vapor, liquid, and uniform heating. They found that when the heat input was purely through the vapor, the pressure rise was much higher than in the case where the heat input was through the liquid. They argued that this was because there was a lot more heat available in the case of vapor heating, whereas in the case of liquid heating, most of the heat input was initially spent in increasing the temperature of the liquid itself. They also found that in the case of uniform heating, the trends were in-between the two extremes. When a subcooled jet was introduced in the setup to increase mixing and minimize pressure build up, they noticed that there was still some noticeable thermal stratification in the liquid. Looking at tank pressurization in reduced gravity using a similar model, Panzarella and Kassemi [24] concluded that buoyancy and natural convection still had a significant role in microgravity conditions. Based on their work with this model, a comparison between typical zero boil off pressure control strategies utilizing different combinations of mixing and cooling was published [25]. Among the different combinations considered, they found that introducing a subcooled mixing jet was the most effective method for controlling the tank pressure rise. Barsi and Kassemi [26] verified this model further by comparing with available experimental data and found reasonable match between the two.

Kassemi and Kartuzova [27] developed a CFD model for solving tank pressurization problems by adopting two different methods to model the interface, viz. a sharp interface and a diffuse interface. The interface mass transfer was calculated based on the Schrage equation. In the case of the sharp interface model the mass transfer was calculated by iterating for the interface temperature by coupling the Schrage equation with a pure conduction energy balance equation at the interface. For the diffuse interface, the mass transfer was calculated by including it in the source term for the

phase evolution equation which was solved as part of the Volume of Fluid (VOF) algorithm. Both these models were verified against the microgravity pressurization data from the Saturn S-IVB AS-203 experiment. It was found that the predictions by the VOF model were much closer to the experimental data than the sharp interface model. They argued that the VOF model was much better at addressing the different aspects of turbulence modeling at the interface. However, they found that the VOF model was much more computationally expensive than the sharp interface model. These models were also used to study the effect of accommodation coefficient and vapor and interface turbulence on tank self-pressurization [28] by comparing with experimental data from NASA's k-site and Multi-purpose Hydrogen Test Bed facilities. It was observed that in the case of a flat interface, the mass transfer rate and pressure rise predictions were quite insensitive to the magnitude of the accommodation coefficient for liquid hydrogen storage tanks.

Stewart and Moder [29] also modeled the k-site tank experiments using a VOF implementation in ANSYS Fluent and have outlined some of the numerical issues encountered while studying a problem of this nature. In order to showcase the current computational ability to capture cryogenic storage tank pressurization, Kassemi et al. [30] compiled and compared three different computational studies highlighting some of the strengths and weaknesses of current modeling techniques for such problems. Kassemi et al. [5] also modeled the Zero Boil Off Tank experiment in both normal and microgravity environments and validated the data against pressurization and jet ullage interaction data from the experiments. They specifically looked at the pressurization behavior under three different heater configurations to simulate the heat leaks expected during normal tank operation in full scale cryogenic storage systems.

Although there have been numerous studies to look at tank self pressurization and pressure control, any such modeling using phase change models without adequately addressing some of the uncertainties inherent in these phase change models would lead to inaccurate predictions in the long run. There are two common strategies used

when modeling interfacial mass transfer in traditional CFD codes. The first one, which is commonly used in near equilibrium conditions, is where the interfacial heat and mass transfer is calculated with the help of a simple conduction based energy balance at the interface. The interface in such a model is assumed to be at the saturation temperature. Such a model tends to give thermally limited predictions for the interfacial phase change rates.

A kinetics based approach to predict phase change was first formulated by Hertz [31]. Assuming a Maxwell Boltzmann distribution for the velocity close to the interface, a theoretical maximum collision frequency can be calculated for the vapor molecules impacting on the liquid-vapor interface. Since evaporation and condensation are coexisting phenomena in near equilibrium conditions, the net phase change flux can be found as an algebraic sum of the two independent fluxes. However, Knudsen [32] based on his experiments with mercury, noted that the measured phase change rates could actually be lesser than the maximum rate predicted by the Hertz equation. In order to account for this discrepancy, he introduced evaporation and condensation coefficients. The most commonly used form of the kinetic phase change models is the model by Schrage [33]. Schrage included a drift velocity term to the equilibrium velocity distribution to account for the non zero velocity contribution coming from evaporation or condensation processes. The Schrage model based on the Hertz-Knudsen-Schrage equation is most commonly used as the kinetic phase change model which is the second approach to model phase change. In this model the interfacial mass flux is calculated based on the difference between the saturation pressure at the interface and the vapor pressure of the gas close to the interface. Essentially, it is a calculation of how far the interface is from equilibrium. These models were initially formulated for a flat interface near equilibrium conditions. The biggest challenge in using the kinetics approach for studying phase change is determining the value of the evaporation and condensation coefficients needed by the model. These coefficients help account for the fact that it is quite probable that a vapor or liquid molecule striking the interface could be reflected back into their initial phases without under-

going phase change. Often the evaporation and condensation coefficients are assumed to be equal and combined to be called the accommodation coefficient.

The accommodation coefficient represents the fraction of molecules that strike the interface and change phase from their initial liquid or vapor states. If every molecule which collided with the interface was to change phase then the accommodation coefficient would be equal to 1. But this is not the case and the reported values for the accommodation coefficient are very inconsistent for any given fluid. For instance, in the case of water the reported values of the accommodation coefficient vary over three orders of magnitude [34]. At the moment, we cannot confidently say much more about the accommodation coefficient. Most of the studies for measuring accommodation coefficient has been for water-water vapor systems. Vieceli et al. [35] calculated the thermal and mass accommodation coefficients for water vapor at the air/water interface using molecular dynamics simulations and determined them to be 1.0 and 0.99 respectively at 300K. Davidovits et al. [36] measured accommodation coefficients for water vapor on water using two different experiment techniques. They noticed that there was a large discrepancy in the measured value of mass accommodation coefficient between the two and attributed this to the difference in the mass accommodation process between the two experiments. Marek and Straub [34] compiled evaporation and condensation coefficients of water from numerous theoretical and experimental studies. Based on this, they concluded that both these coefficients have an inverse dependence on temperature and pressure. They also noted that the measurement of these coefficients is very sensitive to the presence of contaminants. There are other reviews which try to address this large scatter in the reported values for the accommodation coefficient of water. Mozurkewich [37] suggested that if the heat transfer in the system is properly accounted for, the measurements for the condensation coefficient should be near unity. Efforts have also been made to measure the accommodation coefficient for other fluids. Lednovic and Fenn [38] measured evaporation coefficients close to unity for four different fluids, viz. diethylene glycol, glycerine, dibutyl phthalate, and oleic acid. They also noted that there was no varia-

tion in these coefficients with temperature which is contradictory to what Marek and Straub [34] noticed in the case of water. Cao et al. [39] computed the accommodation coefficient for n-dodecane molecules and found that it increased from 0.3 to 0.9 when temperature changes from $600\,K$ to $400\,K$. Paul [40] compiled and collected evaporation coefficients for a variety of metals, inorganic, and organic compounds in a single paper which can be a valuable reference to compare with. Here again he noted that most of the fluids studied evaporate close to the theoretical maximum rate. Barrett and Clement [41] studied accommodation coefficients of water and liquid metals and noted that only at thermal equilibrium can the evaporation and condensation coefficients be guaranteed to be equal. They also found that even the smallest amount of non-condensable gases could significantly reduce the mass transfer rate measurements. Additionally, they found that the accommodation coefficient values could have large discrepancies depending on the nature of the experiment. Accommodation coefficients were often measured to be less than 0.05 in the case of horizontal flat surfaces in comparison to values greater than 0.2 in the case of aerosol growth experiments. This dependence of the accommodation coefficient on droplet size was also observed by Okuyama and Zung [42] in their numerical study to measure these coefficients in the case of water, Helium, and Mercury.

A brief discussion on the drawbacks of the Hertz-Knudsen equation and the accommodation coefficients based on an examination of a variety of experimental, computational, and molecular dynamics studies was published by Persad and Ward [43]. Recently, Davis [44] reviewed the history of research on these accommodation coefficients and looked at the current state of our understanding about them. However, there have not been many studies to deduce the value of these accommodation coefficients for cryogenic fluids. With the emphasis on long duration cryogenic storage for large scale space exploration and the need for designing these capabilities with computational tools, it is imperative that there is a better understanding of these coefficients and their values. Without accurate values for the accommodation coefficient, any reduced order model is an attempt to mimic an already inaccurate model,

and thus, are doomed to perform poorly. Hence, using these models to design cryogenic propellant tank systems might not be very reliable. In order to better study accommodation coefficients, it is important to have purpose-built experiments (Appendix A) with data which would help reduce some of the uncertainties surrounding these coefficients. Since earth bound measurements of accommodation coefficient are ambiguous and are affected by convective heat and mass transfer due to gravity, the no convection, or zero gravity accommodation coefficient needs to be measured using an experiment which has a negligible or known non-zero vapor phase convection. It is important to investigate the true accommodation coefficient in the absence of convective heat and mass transfer for several reasons. Zero-gravity coast periods minimize vapor phase convection, and only an accommodation coefficient measured in the absence of vapor phase convection can be used to model these conditions. For example, convection increases the system scale evaporation rate and if not accounted for properly in experiments any derived values for the coefficient will be wrong. An experiment design to produce steady repeatable vapor flow over a cryogenic droplet is presented in Appendix A.

Bellur et al. [18] also developed a combined experimental and computational approach to determine the accommodation coefficient for liquid hydrogen and liquid methane. The experiment used neutron imaging to image evaporating and condensing menisci for these cryogenic propellants in metallic containers. In the latter chapters of this thesis, data from this experiment is used to compare with full CFD computations for phase change predictions.

2.1 Numerical Model

In this section, we will look at the governing equations and their numerical implementation to solve for the fluid and solid regions. The conjugate heat transfer solver ChtMultiRegionFoam available as part of the standard OpenFOAM [45] distribution is used as the base for all phase change computations. Since a conjugate heat transfer

solver is used, the solid and fluid regions are solved separately adhering to prescribed boundary conditions at the interfaces.

2.1.1 Governing Equations

The fluid flow and heat transfer in the fluid regions are solved with the help of the continuity (mass), Navier Stokes (momentum), and energy equations. These equations are solved separately for the two fluid regions (i.e., vapor and liquid).

$$\frac{\partial \rho}{\partial t} + \nabla(\rho v) = 0 \tag{2.1}$$

$$\frac{\partial}{\partial t}(\rho v) + \nabla(\rho vv) = -\nabla P + \nabla(\mu_{eff}(\nabla v + \nabla v_T)) + \rho g + F_v \tag{2.2}$$

$$\frac{\partial}{\partial t}(\rho E) + \nabla(v(\rho E + P)) = \nabla(k_{eff}\nabla T) \tag{2.3}$$

In the solid regions, a simple conduction equation is solved for the energy equation. This computes the heat conduction in the respective solid regions.

$$\frac{\partial}{\partial t}(\rho C_p T) = \nabla(k\nabla T) \tag{2.4}$$

In this study, the interface is treated as a sharp interface with zero thickness and the interface mass transfer is computed two ways viz., the thermally limited model and the kinetically limited model. Since we are dealing with sharp interfaces both these models can be solved directly over the standard governing equations. The thermally limited model performs a simple conduction based energy balance at the interface.

$$\dot{m}L_b = q_{il} - q_{iv} = k_v\nabla T_v - k_l\nabla T_l \tag{2.5}$$

where L_b is the latent heat of vaporization of the liquid; $\dot{m}$ is the interfacial mass transfer rate; q_{il} and q_{iv} are the corresponding heat fluxes on the liquid and vapor sides; k_l and k_v are the thermal conductivities for the liquid and the vapor side; and

T_l and T_v are the liquid and vapor temperatures respectively. The model essentially states that the difference between the heat flowing in and the heat flowing out at the interface is spent for phase change. In this model we assume that the interface temperature is known, and is equal to the saturation temperature of the gas corresponding to its vapor pressure. Knowing the interface temperature, the mass transfer rate can then be easily calculated as all the other quantities are known. This model works really well at conditions close to equilibrium and is the simplest way to look at phase change at the interface.

On the other side, the kinetically limited model which we call the Langmuir model makes use of the Hertz-Knudsen-Schrage equation. This equation has become the most widely used method when computing phase change problems using kinetic models.

$$\dot{m} = \left(\frac{2\alpha}{2-\alpha}\right)\sqrt{\frac{M_v}{2\pi R}}\left(\frac{P_i}{\sqrt{T_i}} - \frac{P_v}{\sqrt{T_v}}\right) \tag{2.6}$$

where, α denotes the accommodation coefficient; M_v is the molecular weight of the vapor; R is the universal gas constant; P_i and P_v are the interfacial and vapor pressures; and T_i and T_v are the interfacial and vapor temperatures. Unlike the thermal model, there is no condition imposed on the interface temperature in this case but we assume that $P_i = P_{sat,i}$. The saturation pressure is calculated based on the Clausius Clapeyron equation.

$$P_{sat,i} = P_0 \exp\left(\frac{-L_b}{R}\left(\frac{1}{T_i} - \frac{1}{T_b}\right)\right) \tag{2.7}$$

where, P_0 is some reference pressure; and T_b is the saturation temperature at the reference pressure P_0. The phase change rates predicted by the kinetic model should asymptotically approach the thermally limited value as the phase change becomes thermally limited. The difference between the phase change predicted by the thermal model and the actual evaporation will be a function of the accommodation coefficient. The kinetic model based on the Hertz-Knudsen-Schrage equation also predicts twice

the phase change flux at an accommodation coefficient of 1 in comparison to the kinetic model based on the Hertz-Knudsen equation.

2.1.2   Numerical Implementation

The governing equations are implemented using existing tools in OpenFOAM [45]. The conjugate heat transfer solver, ChtMultiRegionFoam, is used as the basis for building additional models necessary to compute phase change. The base solver is not inherently designed for modeling a liquid vapor interface and hence additional boundary conditions are necessary to model the heat, mass, and momentum transfer at the interface. The mass flux and the interface temperature are defined in the liquid domain and are used to calculate the velocities and temperatures on both sides of the interface. Due to the incompressible treatment of the liquid, the velocity on the liquid side due to phase change is considered to be zero. In the case of the conjugate heat transfer solver, there is no inbuilt algorithm for tracking the interface such as the Volume of Fluid (VOF) method and the interface is treated as a static sharp interface separating the two blocks for the liquid and vapor regions. As a consequence, an additional boundary condition is defined to account for the Laplace pressure jump across the interface which would come into effect due to the curvature of the interface. The phase change equations are solved in addition to the standard governing equations every time step to update the velocity and temperature field at the interface. The thermally limited evaporation model can be directly used to calculate the mass flux at the interface, as the interface temperature is already known to be equal to the saturation temperature corresponding to the sampled vapor pressure.

The Langmuir model on the other hand, is a bit more complicated to implement. There are three unknowns in the Hertz-Knudsen-Schrage equation which need to be addressed, viz., the mass flux, accommodation coefficient, and the interface temperature. The accommodation coefficient is given as an input to the solver as it is the parameter we expect to adjust in order to match the phase change rates. Since

the interface temperature in this case is not restricted to be equal to the saturation temperature, we need to define ways to calculate the interface temperature before calculating the interfacial mass flux. In this study we look at two different ways to compute the interface temperature with varying degrees of success. To compute the interface temperature, we combine the Hertz-Knudsen-Schrage equation with the interfacial energy balance equation and iterate for the interface temperature which would be the only unknown in the equation. There is no restriction imposed on the interfacial temperature in this case. The iteration is done by means of the bisection method which has been found to be the more stable method. Once the interface temperature is calculated, the mass flux can then be computed directly from the Hertz-Knudsen-Schrage equation for given values of the accommodation coefficient.

Other methods to compute the interface temperature are attempted to a lesser degree of success. For instance the temperatures from the cells adjacent to the interface on both the liquid and vapor side are sampled and the interface temperature is set to be equal to the average of the liquid and vapor temperatures. This is expected to be a lot less accurate than the iteration method as the temperature gradients leading to the interface are not correctly accounted for. Interpolating the temperatures from the liquid and vapor side on to the interface and then averaging them might improve the estimate for the interface temperature. In all calculations presented, the pressure velocity coupling is done using the PISO algorithm. The gradients are calculated with the Gauss Linear scheme. The Gauss upwind scheme is used as the divergence scheme and a second order linear interpolation scheme is used for pressure and flux interpolation. In the following chapter, a sample benchmark case is introduced and the phase change models described above are evaluated and compared to get some initial trends for these models.

3. BENCHMARK CASES

In order to evaluate the phase change models implemented into OpenFOAM, a benchmark case is established as shown in Figure 3.1 representative of the test section in the experiment described in Appendix A. A simple two dimensional test case of a liquid drop in a silver cup with vapor flow over it is used for this purpose. The fluids used in this test scenario are water and water vapor. A flat interface is considered to simplify the problem, as this let us evaluate phase change without the effects of interface curvature. Using a perfect fluid equation of state model for the liquid causes convergence issues near the contact line. Hence, the liquid is treated as a constant density region until the variable density models in OpenFOAM are properly evaluated. Viscous coupling at the interface is also not accounted for at this stage and the liquid region is modeled similar to a rigid solid body with no internal flow.
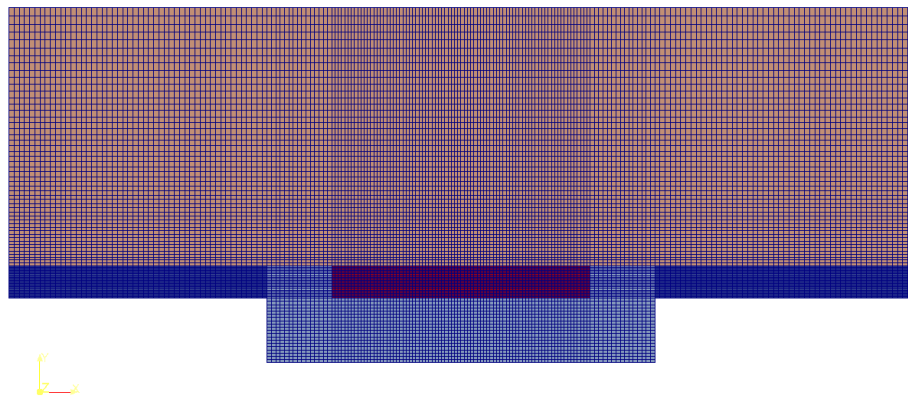
Figure 3.1. Two-dimensional grid for the benchmark case (16900 cells). Regions: orange = vapor; red = liquid; dark blue = stainless steel wall; light blue = silver cup.

Separate computations were carried out for evaporation and condensation. Evaporation is induced by setting the bottom surface of the silver cup at a constant temperature of $400\,K$ and letting the heat conduct through the silver and the liquid regions to the liquid-vapor interface. Similarly, for condensation the bottom boundary of the silver cup is maintained at $350\,K$. Vapor is allowed to flow over the liquid droplet at a constant velocity of $5\,cm/s$. The bulk temperature is set to $370\,K$ corresponding to the saturation temperature at the prescribed vapor pressures.

Looking at the temperature contours presented in Figure 3.2, we can see the temperature rise through the regions because of heat conduction from the base of the silver cup. Initially at start up, we have condensation due to the low temperatures at the liquid-vapor interface. But as the liquid heats up due to conduction from the silver cup, the phase change at the interface slowly changes to evaporation, which can be seen represented by the velocity vectors at the interface. Since we are dealing with a flat interface, the velocities at the interface due to phase change are strictly in the vertical direction (y-coordinate). It is also seen that the heat conducts much faster through the silver cup than the liquid. This is expected due to the higher thermal conductivity of silver compared to water.

Computations were run for 60 seconds till the heat was conducted fully to the interface. It would be interesting to see the effects as heat is continued to be supplied for longer periods of time. Using the Langmuir model, the accommodation coefficient is varied to study its effect on the interfacial mass transfer. Computations were run for evaporation and condensation with $\alpha = 0.6, 0.06, 0.006, 0.0006, 10^{-6}$, and 10^{-9}. Comparing the mass transfer rate at the interface with the thermally limited model, there are some very interesting trends noticed. The mass transfer rate is recalculated by integrating the velocity over the interface during post processing.

It is observed that the interfacial mass flux calculated using the iteration method for accommodation coefficients $\alpha = 0.6, 0.06$, and 0.006 are almost identical to the value calculated by the thermally limited model. The variation of mass flux with time is also identical for these values of accommodation coefficient as shown in Figure 3.3.

(a) Time = 0s

(b) Time = 10s

(c) Time = 20s

(d) Time = 30s

(e) Time = 60s
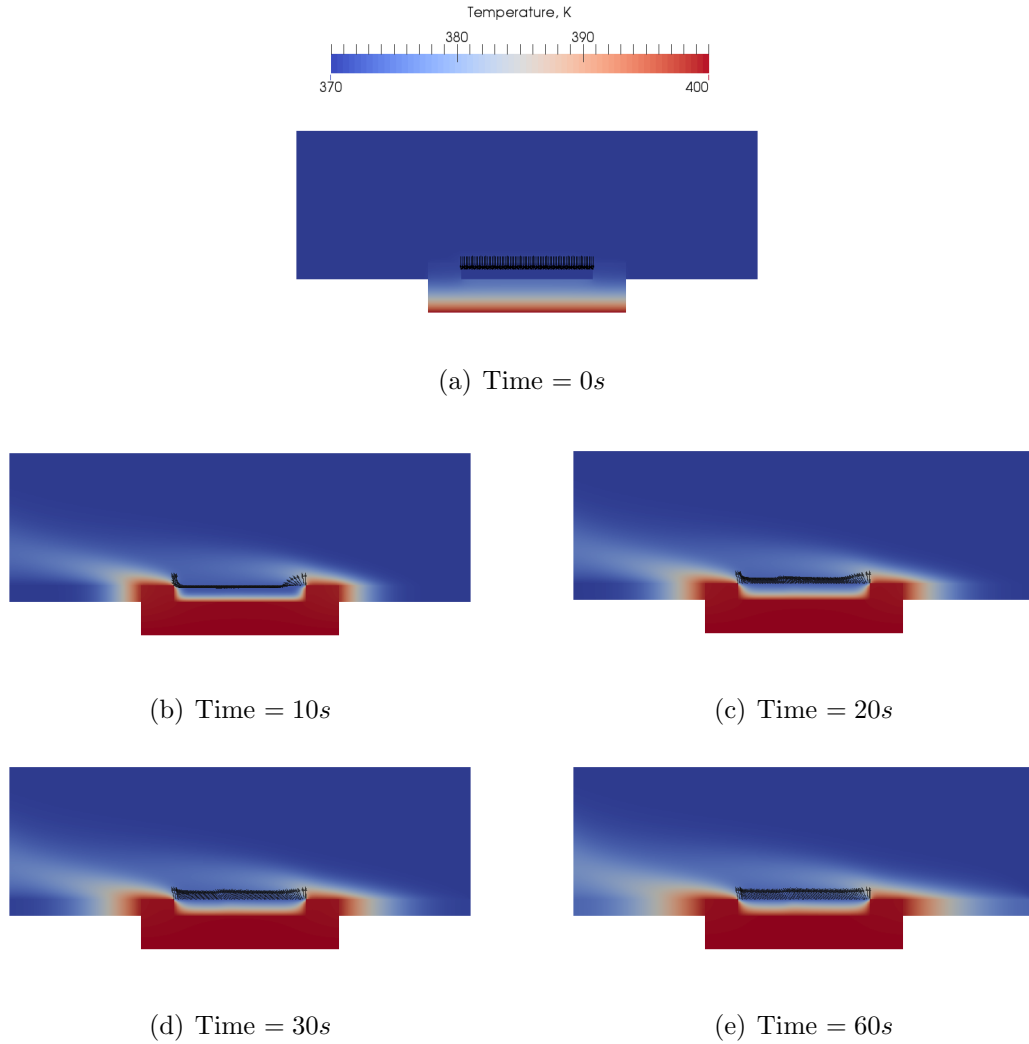
Figure 3.2. Langmuir model applied to 2D benchmark case with $\alpha = 0.6$. Velocity vectors at interface show initial condensation and eventual progression to evaporation. The temperature contours are presented to show heat conduction through the different regions. The interface temperature is calculated by the iteration approach. The bottom surface of the silver cup is maintained at $400\,K$.

When the accommodation coefficient is further reduced by an order of magnitude to 0.0006, the interfacial mass transfer rate values calculated start to deviate from the predictions of the thermally limited model. This deviation is much higher at lower values of accommodation coefficients of 10^{-6} and 10^{-9}. The mass flux reduces as many orders of magnitude as the accommodation coefficient at these low values of

accommodation coefficient. It remains to be seen if this deviation in the interfacial mass flux at lower accommodation coefficients is because of the phase change at these low values of accommodation coefficient being kinetically limited, whereas at higher values of accommodation coefficient, the phase change is still thermally limited. Generally, for moderate accommodation coefficients the transport rates are much slower than the kinetics and the overall mass transfer rate might not change much until the two are approximately the same orders of magnitude. Further investigation is required to see if this is the reason behind such trends.

To explain the similarities in the variation of mass flux between the iteration method and the thermally limited model, we look at the difference between the saturation pressure (based on the interface temperature) and the actual vapor pressure at the interface. This constitutes the second term of the Hertz-Knudsen-Schrage equation and its variation might throw some light on these trends. It is apparent from the plots in Figure 3.4 that the change in accommodation coefficient is balanced by the change in the saturation pressure. Such a change in saturation pressure means that the interface temperature adjusts itself to compensate for the change in the value of the accommodation coefficient. For instance, the interfacial pressure difference for an accommodation coefficient of 0.0006 is an order of magnitude higher than for an accommodation coefficient of 0.006. Thus a change in the accommodation coefficient is generally compensated by a change in the interfacial pressure difference so that the same interface mass transfer rate is predicted. This was also observed by Kassemi and Kartuzova [28] in their investigation on the effect of the accommodation coefficient on CFD predictions of tank pressurization.

It is important to note that the interface temperature used here for calculating the interface saturation pressure is an average temperature over the whole liquid-vapor interface. However, in reality there is a variation in the interface temperature along the interface with higher temperatures close to the ends in contact with the silver cup and lower temperatures in the middle. The corresponding saturation pressure also varies along the liquid-vapor interface. This difference in temperature is because

of the faster heat conduction through the silver which causes the temperature at the liquid-vapor-silver junction to be much higher than the bulk liquid temperature. The mass transfer rates calculated at the interface for condensation, using the iteration method, also show similar trends as evaporation. Condensation is induced at the interface by maintaining the bottom surface of the silver cup at $350\,K$, keeping all other conditions the same. Comparing the mass transfer rates predicted for this case with the thermally limited phase change model, it is seen that the mass transfer rates for higher accommodation coefficients ($\alpha = 0.6, 0.06$, and 0.006) are equal to the mass transfer rates from the thermally limited model. Here again, the interface temperature adjusts itself to balance out the change in accommodation coefficient. At an accommodation coefficient of 0.0006, the mass transfer rates start deviating from the predictions by the thermally limited model. It will be interesting to see if this shift in mass transfer rate predictions with varying values of accommodation coefficient differs for different fluids.

The second approach to model the Hertz-Knudsen-Schrage equation for interfacial mass transfer prediction is by averaging the temperatures from the liquid and the gas regions to get the interface temperature. This temperature is then directly used in the Hertz-Knudsen-Schrage equation to compute the interfacial mass transfer rate. Again, the mass transfer rates predicted by the Hertz-Knudsen-Schrage equation are compared with the predictions of the thermally limited phase change model. In this approach we find that the magnitude of mass flux is much higher than that predicted by the iteration approach for the same accommodation coefficient and conditions. Also, unlike the iteration approach the mass transfer rate is also higher than the predictions from the thermally limited model by at least a few orders of magnitude. The variation of interfacial mass flux with time is also different for different accommodation coefficients unlike the earlier approach. This method is highly computationally intensive due to the very high interfacial mass transfer rate values which in turn lead to very high interfacial velocities. The model does perform better at lower values of accommodation coefficient with the mass transfer rates predicted within one order of

magnitude to the thermally limited calculations for an accommodation coefficient of 0.0006. For accommodation coefficients of 10^{-6} and 10^{-9}, the mass flux predictions show very similar trends to the calculations from the iteration approach. However, this seems like a really low value for the accommodation coefficient as the estimated value for the accommodation coefficient of water is close to 1. The interface temperatures follow similar trends for varying values of accommodation coefficient. For the higher values of the accommodation coefficient, there is quite a deviation from the temperatures calculated by the iteration approach. This deviation becomes smaller and smaller with the lower values of accommodation coefficient showing nearly identical temperature transients for both the models.

Based on the data presented here the iteration approach seems to be the better of the two with more realistic predictions in terms of temperatures. But, looking at mass transfer rates and comparing it with a thermally limited mass transfer rate is not the best method to evaluate the performance of these models. It might be a better option to look at more physical data from specifically built experiments or studies such as tank pressurization experiments and try to match the data with these models.
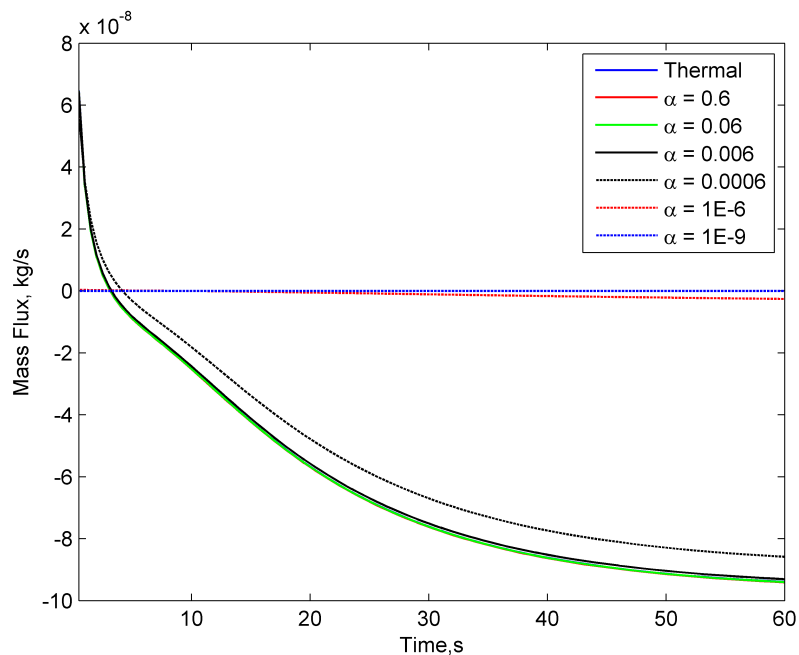
(a) Evaporation
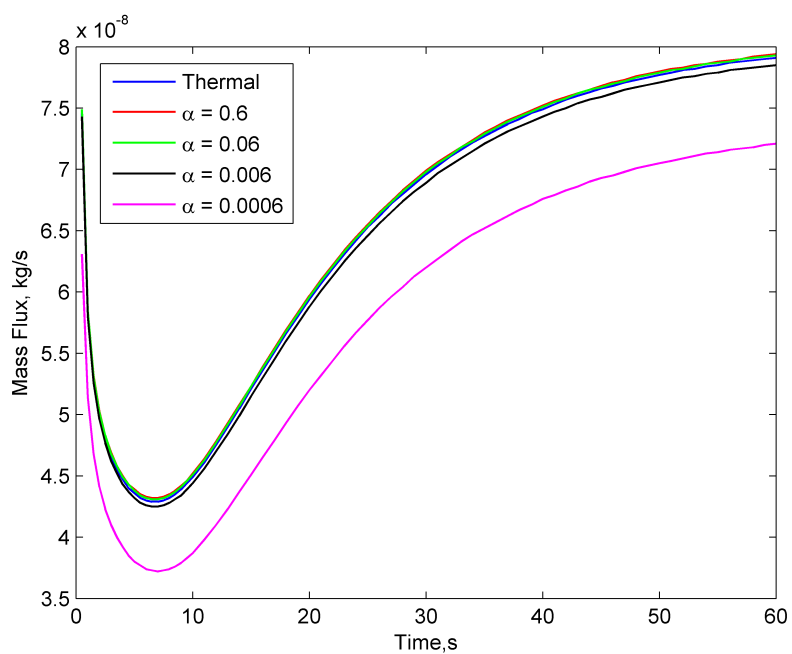
(b) Condensation

Figure 3.3. Evolution of interfacial mass flux with time for varying accommodation coefficients. Comparisons made with predictions of thermally limited model.
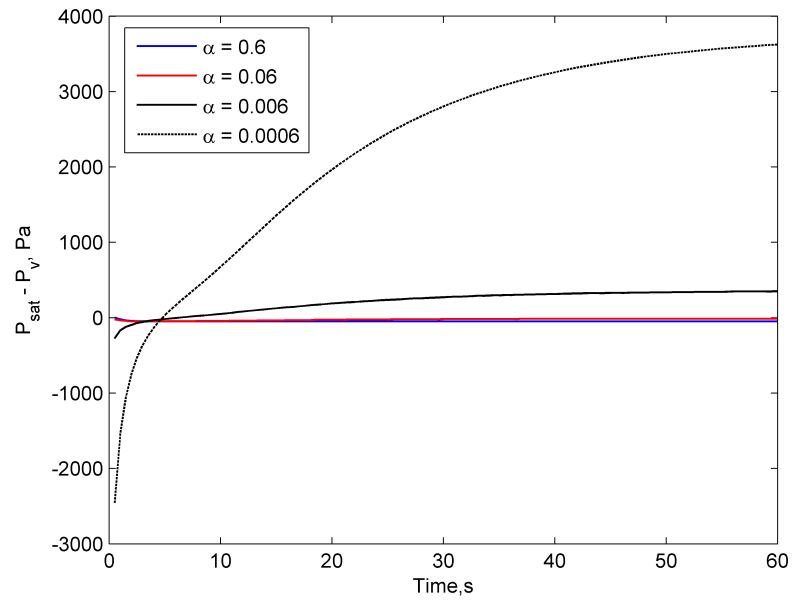
(a)
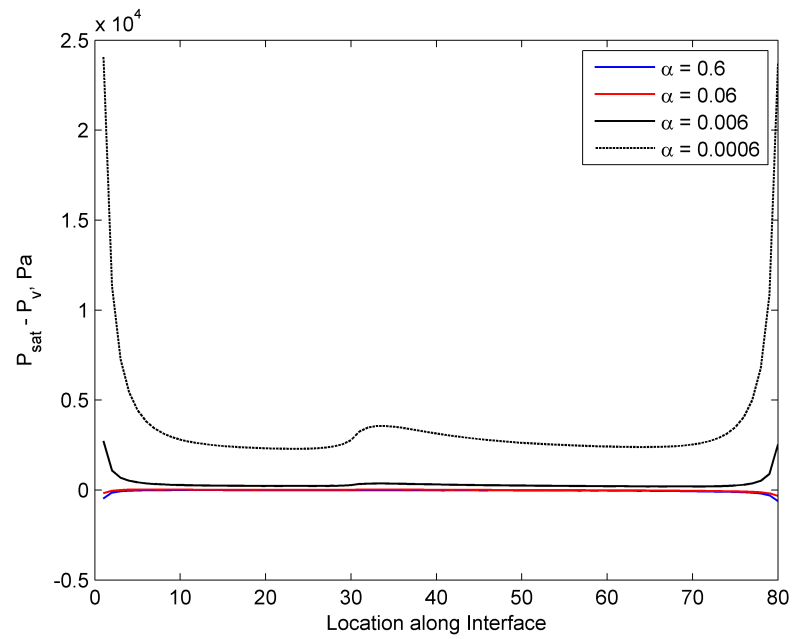
(b)

Figure 3.4. Variation of $P_{sat} - P_v$ with (a) time and (b) location along the interface for varying accommodation coefficient.
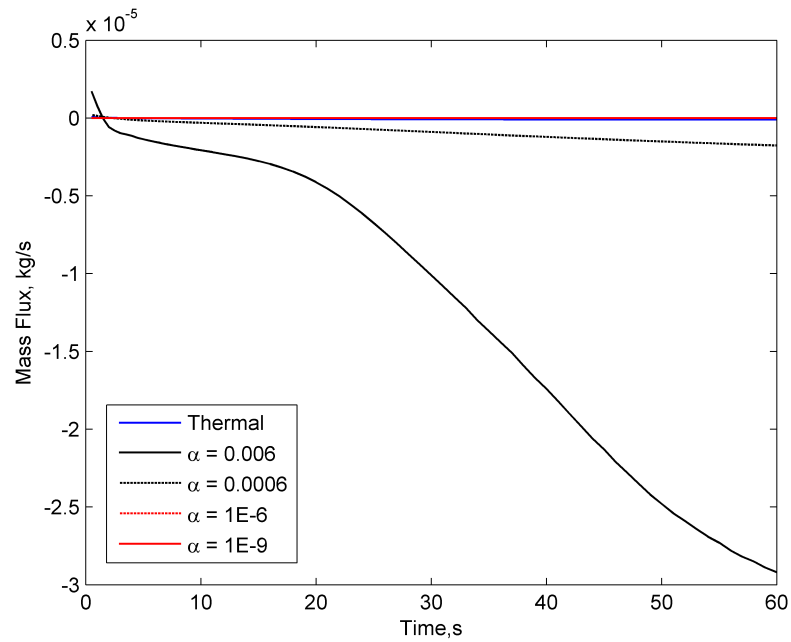
(a)
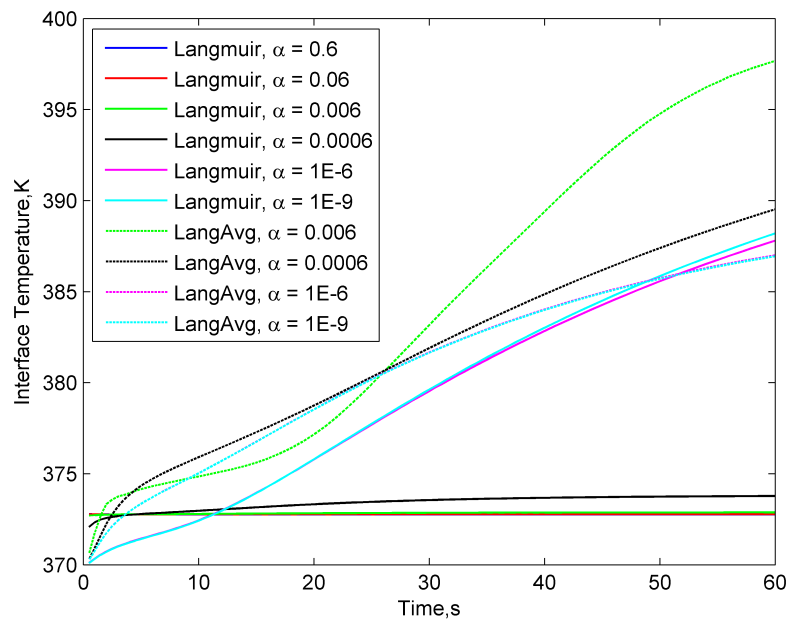
(b)

Figure 3.5. (a) - Mass transfer rate prediction using the averaging approach to calculate interface temperature. (b) - Comparison of interface temperature values calculated by the iteration and averaging methods.

4. MODELING OF THE NIST LH2 EXPERIMENT

Having checked the solver with a sample benchmark case as described in the previous chapter, it is now important to verify the accuracy of the models incorporated into OpenFOAM with some experimental data. Experimental data for pure liquid vapor systems are almost non-existent as phase change and accommodation coefficients are often studied for water-air systems or systems which have some non-condensable gas present in the vapor phase. Since the OpenFOAM solver in its current state does not have species tracking, such experiments cannot be used for validation. Moreover, experiments studying phase change in cryogenic fluids are not widely available. The k-site tank experiments were considered as a potential test case, but given the simplifying assumptions in the solver we would not be able to account for viscous coupling and thermal stratification in the tank. The experiments by Bellur et al. [46] performed at NIST designed to measure accommodation coefficients for cryogenic hydrogen and methane with the help of neutron imaging provide us with a possible test case at a much smaller length and time scale than full scale tank experiments.

This experiment makes use of the difference in the scattering behaviour of thermal neutrons between these cryogens and other materials in order to image the liquid-vapor interface. The test cell, within which the cryogens are contained, is a $10\,mm$ diameter cylindrical aluminum vessel that is attached to the end of a sample stick and inserted into NIST's orange cryostat. The orange cryostat has an annular arrangement with alternating LN2 and Helium sections to cool the system to the required temperatures. The data from the LH2 experiments are used in this chapter to draw comparisons with computational predictions. Both evaporation and condensation studies were performed with this setup. Based on the location of the interface, tracked using neutron imaging, the interface coordinates, liquid volume, and phase

change rates were obtained from the experiment. The test cell and the different components around the test cell are shown in Figure 4.1
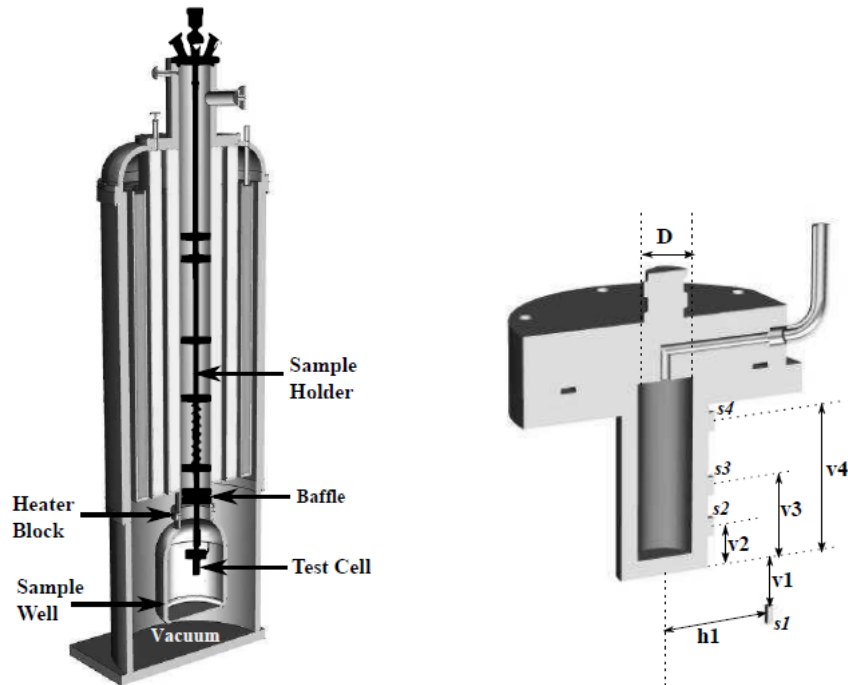
Figure 4.1. (a) Cut section model of full experimental setup. (left) (b) Test cell with lid showing location of temperature sensors and pressure vent (right) (from Bellur [47]).

Evaporation and condensation in the test cell was induced by controlling the temperature of the heater block, which is located away from the test cell, while keeping the test cell vapor pressure constant. There are two main heat transfer pathways to the liquid-vapor interface for phase change as outlined by Bellur [47] viz. heat conducted through the solid regions to the top of the test cell lid and also conduction/convection through the helium in the can surrounding the test cell. The test cell was surrounded by Helium to improve the heat transfer and reduce the time taken for the heat to conduct to the interface. There is however no information about the pressure or the density of the helium in the sample well can.

Temperatures were measured on the side wall of the test cell with three temperature sensors. A fourth sensor was placed in the sample well a little distance away from the test cell wall to measure the temperature of the helium at that location. The exact sensor locations are shown in Figure 4.1. The four sensors were Lakeshore DT-670 sensors which have an uncertainty of about $\pm 0.25\,K$. There was an additional temperature sensor on top of the test cell lid which would give us additional temperature data for our computations. This sensor however was less accurate and had an accuracy of $\pm 1\,K$. The pressure on the vapor side in the test cell was held constant with a throttling mechanism and was also measured with an uncertainty of about 0.2%. The computations presented in this thesis, focused on just the test cell and the lid and imposed boundary conditions for temperature and pressure to fully define the thermal state of the system.

4.1 Computational Model of the Experiment

From the experiments conducted at NIST by Bellur et al. [46], it was found that the liquid-vapor interface in the case of the two cryogens was almost a zero degree contact angle interface as shown in Figure 4.2. Modeling a zero degree contact angle interface as a sharp interface, as in the OpenFOAM solver, presents a multi scale problem where there will be really small cells near the contact line. Modeling all the different length scales would be almost impossible within reasonable computational resources. The coordinates for the liquid-vapor interface for an experimental Bond number of 9.3 are obtained by solving the Young-Laplace equation and the data is corroborated with experimental images. These coordinates are then imported into the OpenFOAM mesh as discrete points and joined together with a spline curve to form the liquid-vapor interface. A sharp contact was maintained at the contact line to start with in order to evaluate the behaviour.

Being a zero degree contact angle interface, it also becomes important to calculate the interface curvature to compute the Laplace pressure jump across the interface.
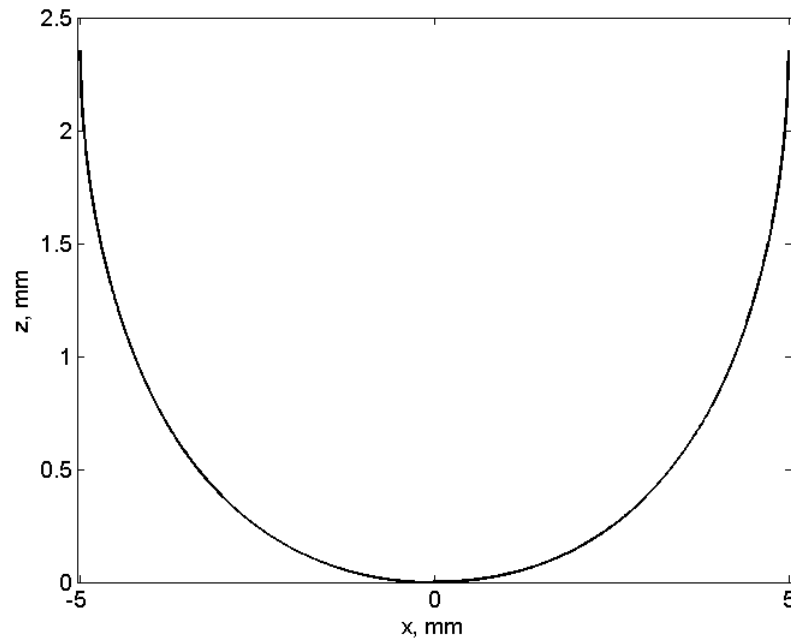
Figure 4.2. Interface coordinates for a zero degree contact angle interface computed from the Young-Laplace equation.

The OpenFOAM solver takes a single fixed value for the Laplace pressure jump as a boundary condition to ensure pressure balance at the interface. The interface curvature was calculated for an axisymmetric surface [48] based on the point coordinate data that was available for the interface. The Bond number in these experiments was calculated to be equal to 9.3, which would lead to varying interface curvature with a slightly flatter region near the middle. The Laplace pressure jump, as a consequence, would also vary across the interface at different locations. Hence, an average value for the interface curvature was used to approximate the pressure jump for the whole interface. But owing to the problems with the variable density models in OpenFOAM, the computations presented here treat the liquid as an incompressible fluid. Based on the Rayleigh and Peclet numbers for this particular experiment, Bellur [47] argued that conduction would be the major heat transfer mechanism to the interface on the

liquid side. Hence, the Laplace pressure jump is not expected to have a major effect on the phase change predicted.

$$\kappa = \begin{cases} \dfrac{z_x}{2x(1+z_x{}^2)^{\frac{1}{2}}} + \dfrac{z_{xx}}{2(1+z_x{}^2)^{\frac{3}{2}}} & \text{when z = f(x)} \\[3mm] \dfrac{z_{xx}}{2(1+z_x{}^2)^{\frac{3}{2}}} - \dfrac{1}{2z(1+z_x{}^2)^{\frac{1}{2}}} & \text{when x = f(z)} \end{cases} \tag{4.1}$$

The test cell was modeled as an axisymmetric problem to save on computational time and resources as shown in Figure 4.3. Since there was no interface tracking built into the OpenFOAM solver, the experiment was modeled as a quasi-steady problem. A volume of $0.814\,cm^3$ was picked and both evaporation and condensation mass fluxes were calculated for the system at this volume. A quadratic fit was used for the side wall temperature based on the temperature data from the three sensors. A constant temperature boundary was used for the top of the lid with the stick sensor temperature data. All other external walls were considered to be adiabatic. These temperature boundary conditions should help account for the two main heat transfer pathways to the liquid-vapor interface as mentioned previously.

In the experiment, there was a pressure vent through the lid of the test cell in order to control the pressure levels in the cell. This line is asymmetric and goes out through the side of the lid. In an axisymmetric model, taking the pressure vent through the side of the lid as in the experiment creates a thin layer of gas between two solid regions. Since conduction through the solid regions is an important heat transfer pathway to the test cell, having a thin layer of gas in-between would affect the solution. The pressure vent was also necessary as the pressure in the test cell would rise in its absence. Thus, a decision was made to have the pressure vent go straight out through the top of the lid. This cuts into the boundary on the top of the lid and reduces it by about 10% but it seemed to be the best solution for an axisymmetric model. The pressure in the test cell is maintained at $121.4\,kPa$ for these calculations which corresponds to a saturation temperature of $21\,K$. However, there is significant fluctuation in the pressure measurement as shown in Figure 4.4
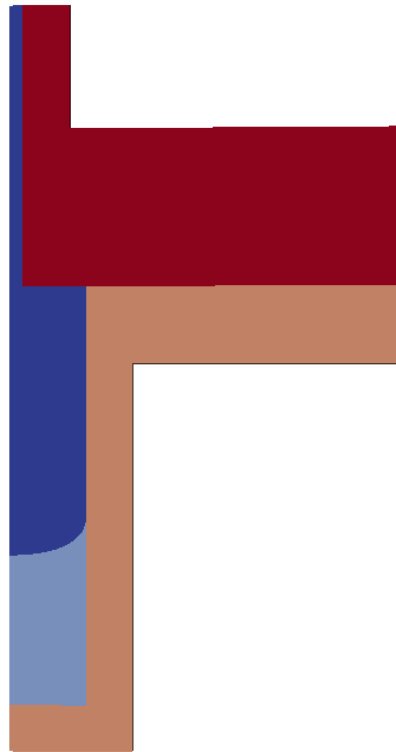
Figure 4.3. Axisymmetric model of the test cell showing different regions. Dark Blue - Gas, Light Blue - Liquid, Dark Red - Lid, and Light Red - Test Cell Wall.

due to the nature of the throttling mechanism. Using a finer needle valve should help reduce this uncertainty further.

The thermophysical properties for the solid regions, Aluminum 6061 and Stainless Steel 316L for the test cell wall and lid respectively, have to be measured at the low temperatures prevalent in the cryostat [49]. The properties of these metals were found to vary quite a lot at these low temperatures as shown in Tables 4.1 and 4.2 and would hence affect the phase change computations.
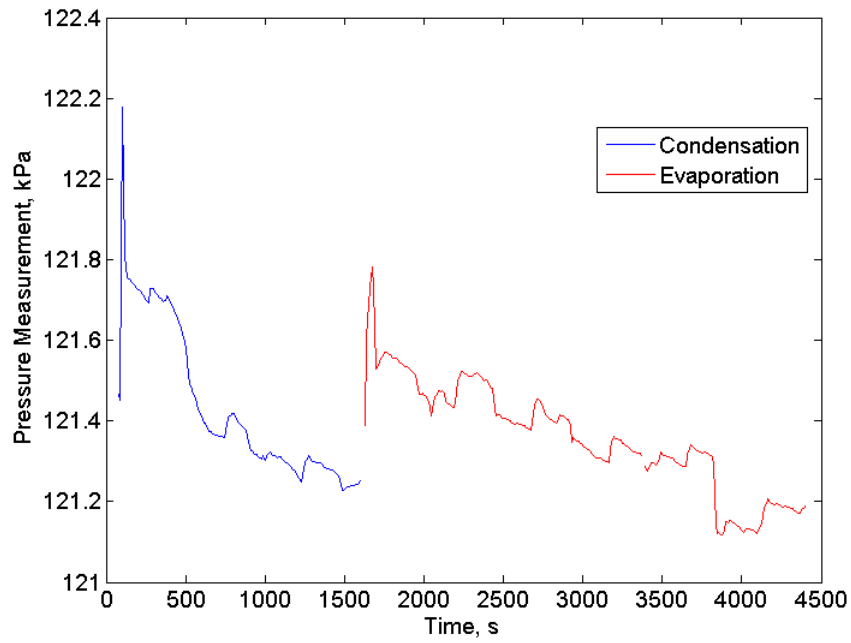
Figure 4.4. Pressure measurement plotted against time showing fluctuation due to the throttling mechanism.

Table 4.1. Properties of Aluminum 6061 at cryogenic temperatures. Data presented from [49].

Temperature (K)	Thermal Conductivity (W/mK)	Specific Heat (J/kgK)
10	14.2	1.573
20	28.43	8.854
40	52.23	81.96
60	70.76	223.6
80	85.56	368.7
100	97.7	492.2

Table 4.2. Properties of Stainless Steel 316L at cryogenic temperatures. Data presented from [49].

Temperature (K)	Thermal Conductivity (W/mK)	Specific Heat (J/kgK)
10	0.9039	5.203
20	2.169	13.61
40	4.670	57.55
60	6.647	141.8
80	8.114	214.7
100	9.224	273.0

4.2 Grid Independence Study

The evaporation case was run on a number of grids to study the grid independence. A sharp contact was maintained at the contact line to begin with. Grids with uniform cell spacing with 14050, 24900, 35856, 56200, and 80676 were used for this purpose. The computations on the grids with 14050 and 24900 produced some fluctuations in the mass flux and did not reach a stable steady state. These non-physical fluctuations are probably caused due to the grid resolution as at higher grid resolutions the model reaches a stable steady state. Uniform grid spacing with simple blocking was used for mesh generation to improve mesh orthogonality. Highly non-orthogonal cells were generated due to the curved interface close to the contact line. The temperature and pressure contours for a sample evaporation test case are shown in Figure 4.5. The data for the evaporation mass flux for these grids using the thermally limited evaporation model is presented in Figure 4.6.

This data is to be compared with the experimental evaporation rate of $55.6\,\mu g/s$ as calculated from imaging data. Looking at the evaporation rate values presented, it can be seen that with increasing grid resolution the evaporation rate keeps going

(a)   (b)
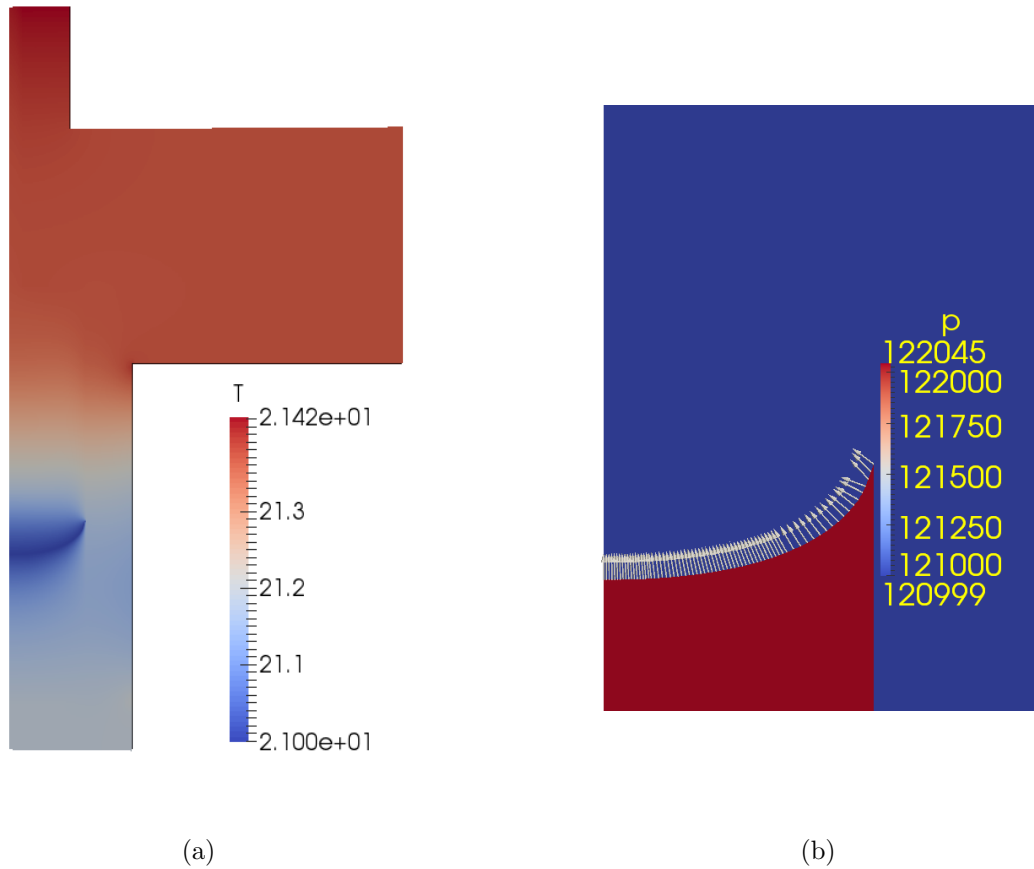
Figure 4.5. (a) Temperature contours for a curved interface model under evaporation. (b) Pressure contours with velocity vectors at the interface showing evaporation.

up and does not necessarily approach a fixed value. This seems to be a consequence of the curved interface. As more and more cells are added to discretize the geometry, the interface becomes better defined and this leads to an increase in the interfacial mass flow rates.

This was verified by running evaporation calculations for a flat liquid-vapor interface model with 6225, 14050, 24900, and 35856 cells. The data for the case with a flat interface is presented in Table 4.3.

From the table, we can quite clearly see the evaporation rates approaching a single value, with increasing grid resolution for a flat interface. With the aim of
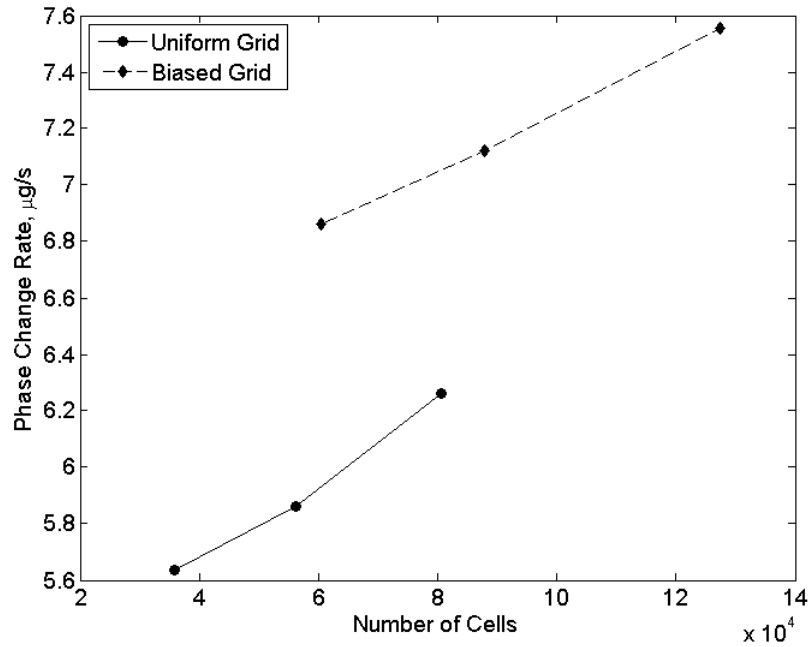
Figure 4.6. Grid independence for curved interface using thermally limited phase change model.

Table 4.3. Grid independence for flat interface using thermally limited phase change model.

# of Cells	Total Mass Flow Rate ($\mu g/s$)
6225	13.8618
14050	14.6237
24900	14.7133
35856	14.2008

improving the solution, non-uniform grids with more cells close to the liquid-vapor interface were created. Grids with 60440, 87880, and 127431 cells were used for these computations. The maximum non-orthogonality in these grids was around 70° and 4 non-orthogonality correctors were used to manage this. The evaporation rate data is

presented in Figure 4.6. Although, grid independence is not achieved even with these grids, they perform much better than the uniform grid setups in terms of mass flux predictions.
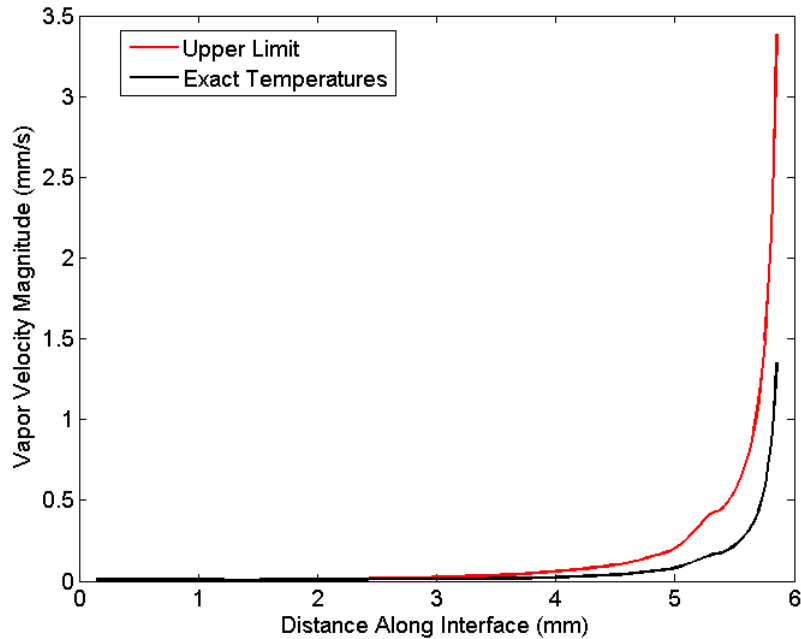
Figure 4.7. Velocity magnitude along the interface shows a spike near the contact line located at $5.9\,mm$.

Looking at the velocity along the interface, as shown in Figure 4.7, the velocity corresponding to the phase change rate at the interface increases close to the contact line. This could be attributed to the relatively smaller thickness of the liquid film and higher heat flux closer to the contact line. Hence, any improvement in the grid resolution would lead to a better prediction of the peak velocity. This could quite possibly be the reason for the grid dependence that we see in the earlier calculations. Besides, modeling all the different length scales in such a multiscale problem is impossible within reasonable computational resources.

To combat the grid dependence problem, a small portion of the interface below a thickness of $10\,\mu m$ was cut out as shown in Figure 4.8. This ensures that the interface
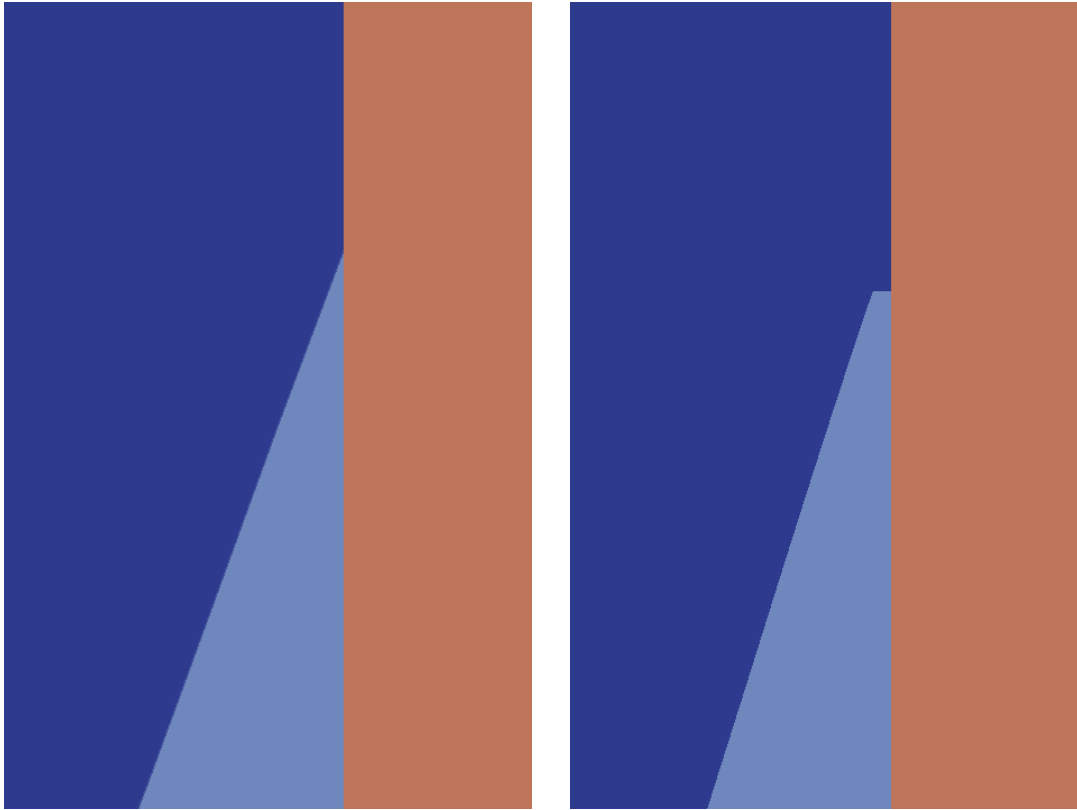
Figure 4.8. Modified interface near the contact line. Left - Interface maintains sharp contact. Right - Interface cut off at $10\,\mu m$.

close to the contact line is flat and also helps set the minimum cell size. With such a setup, grid independence was verified using grids with 66661, 95939, 116916, and 350688 cells. The evaporation rate data, shown in Table 4.4, clearly shows that the evaporation rate does not change with increasing grid resolution. This indicates that the grid dependence in the problem was caused by the region close to the contact line as discussed previously. Looking at the velocity distribution along the interface further reiterates this hypothesis as the velocities are identical in the bulk region of the interface.

The cut off region was also extended to $15\,\mu m$ in order to look at the effect the size of the cut off region has on these calculations. Although as expected, the total evaporation rate is lower due to more of the interface missing, the velocities along the
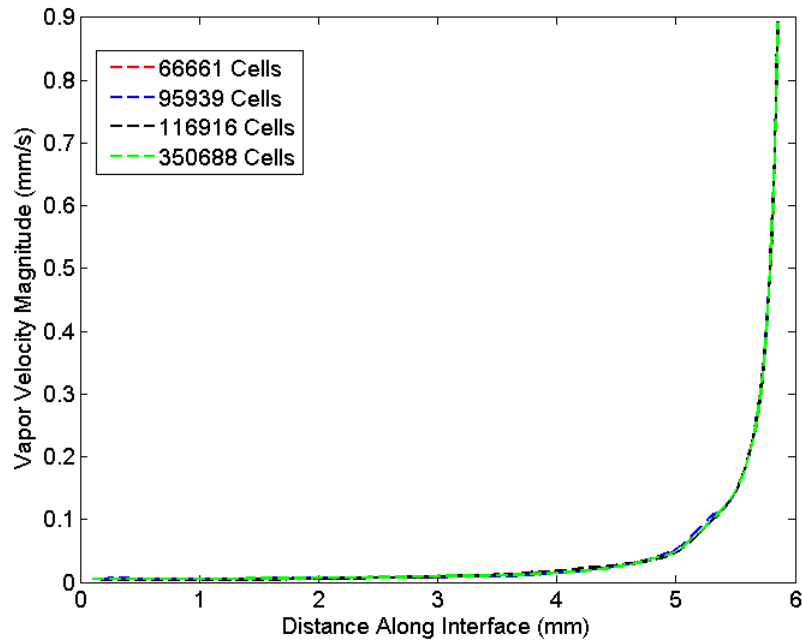
Figure 4.9. Velocity magnitude along the interface for different grids showing grid independence.

Table 4.4. Grid independence for interface cut off at $10\,\mu m$ using thermally limited phase change model.

# of Cells	Total Mass Flow Rate ($\mu g/s$)
66661	9.0322
95939	9.0518
116916	9.0377
350688	9.0245

interface are nearly identical until the cut off portion for the $15\,\mu m$ case in comparison to the $10\,\mu m$ case. This again shows that the grid dependence is due to the better prediction of the peak velocity close to the contact line as the grid cells become smaller in that region.
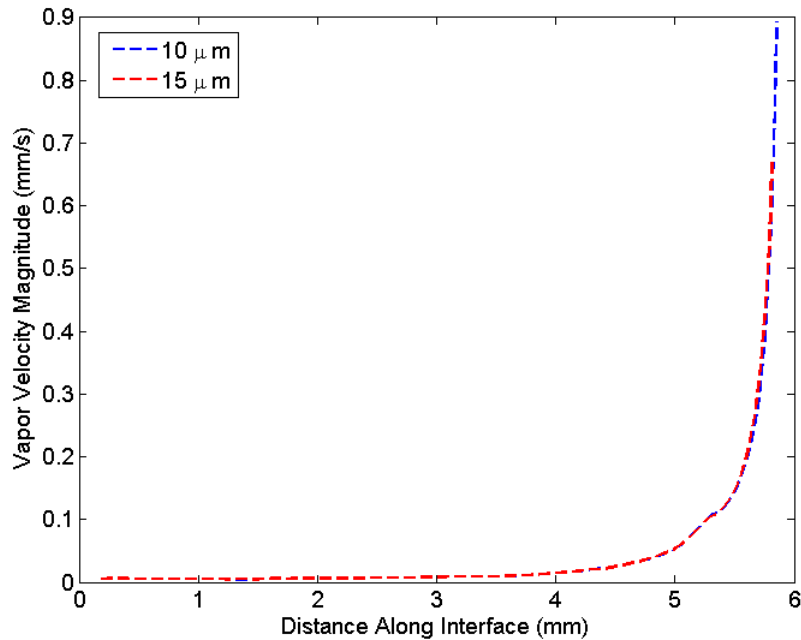
Figure 4.10. Velocity magnitude along the interface for different cut off lengths showing grid independence.

4.3 Effect of Accommodation Coefficient

As grid independence is achieved by cutting the interface at a thickness of $10\,\mu m$, this thickness is used in all computations presented in this dissertation going forward. The grid with 95939 cells is used specifically to save on some computational cost as higher grid resolution does not change the phase change rates which is the quantity of interest. These calculations take 2-3 weeks to reach steady state when run in parallel maintaining 10000 cells/processor.

From the thermal analysis of the experimental setup performed by Bellur [47], it was seen that the temperature measured by one of the temperature sensors (S4) was always $0.5\,K$ above the estimated temperature from the computational model. This difference was attributed to a temperature dependent thermal offset in the calibration of the sensor. This was however not verified with the original temperature sensor.

In the computations presented here, this temperature offset is accounted for while formulating boundary conditions with the temperature measurements from S4.

Evaporation calculations corresponding to a liquid volume of $0.814\,cm^3$ were studied using both the thermal and the kinetic model on this setup to compare with the experimental data. The evaporation rates were computed using the kinetically limited phase change model for four values of the accommodation coefficient spanning four orders of magnitudes. Accommodation coefficient values of 0.6, 0.06, 0.006, and 0.0006 were picked for this purpose. The corresponding evaporation rates are presented in Figure 4.11.
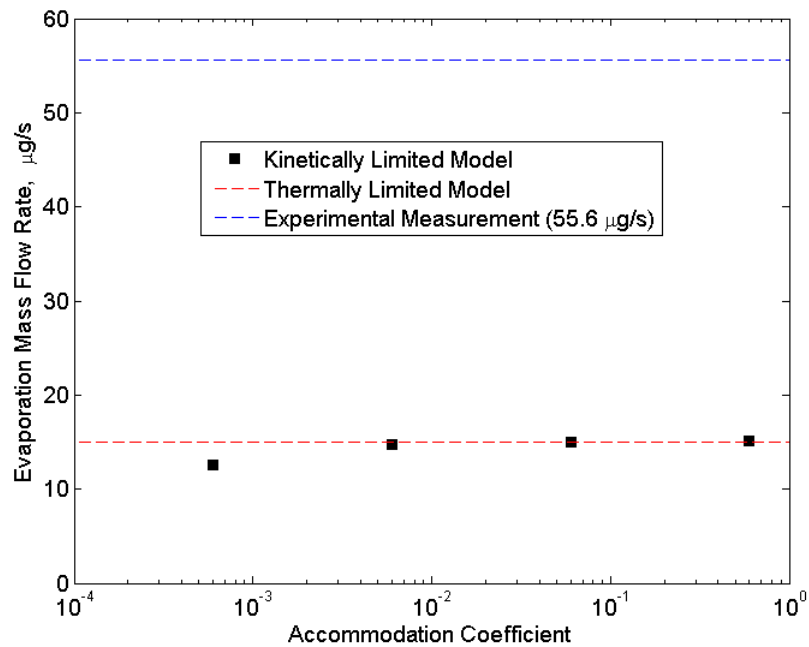
Figure 4.11. Evaporation rate predictions with the thermally limited model and kinetically limited model for varying accommodation coefficients. Experimental measurement $= 55.6\,\mu g/s$.

Looking at the effect of accommodation coefficient on phase change, it is clear that the accommodation coefficient does not have much effect on the evaporation rate for about three orders of magnitude. For accommodation coefficients of 0.6, 0.06, and 0.006 the mass transfer rates predicted are almost identical with very minimal change.

Interestingly, the evaporation rate predicted by the thermally limited phase change model is also close to the predictions of the kinetically limited phase change model at these higher values of accommodation coefficient. As noted previously, this could be attributed to the interface temperature and consequently the interface saturation pressure adjusting itself to compensate for the change in the accommodation coefficient. This could also potentially explain the three order of magnitude scatter that is observed in the value of the accommodation coefficient for a particular fluid. In near equilibrium conditions, such as in this experiment where the temperature difference is the order of $0.5\,K$ or the k-site tank experiments studied by Kassemi and Kartuzova [28], the phase change at the liquid-vapor interface seems to be a thermally limited process. This would explain the independence of the phase change rate predicted with changes to the accommodation coefficient. This would also explain the identical evaporation rate predicted by both the thermally limited and the kinetically limited phase change models.

In fact, at lower values of accommodation coefficient, such as 0.0006 shown in Figure 4.11, there is a deviation in the evaporation rate predicted by the kinetically limited model. This could possibly be due to the phase change becoming a more kinetically limited process at these lower values of accommodation coefficient.

However, in all of these computations the phase change rates that are predicted are still quite low when compared to the experimental measurements. In the following chapter, the reasons for this discrepancy are studied in further detail to bridge the gap between computational predictions and experimental measurements for phase change.

4.4 Condensation Calculations

In the experiment performed at NIST, initially condensation was induced at the liquid-vapor interface by setting the heater temperature below the saturation temperature corresponding to a vapor pressure of $121.4\,kPa$. So at a liquid volume of

$0.814\,cm^3$, the same data required for the computations are available for the condensation case. Using the new temperature and pressure measurements corresponding to the new thermal state of the experiment, boundary conditions are formed to input into the computation model. Condensation rates were calculated using both the thermally limited and the kinetically limited phase change model on the same grid used for the evaporation calculations outlined in the previous section. For the kinetically limited phase change model, the accommodation coefficient was varied by four orders of magnitude viz., 0.6, 0.06, 0.006, and 0.0006 like in the case of evaporation.
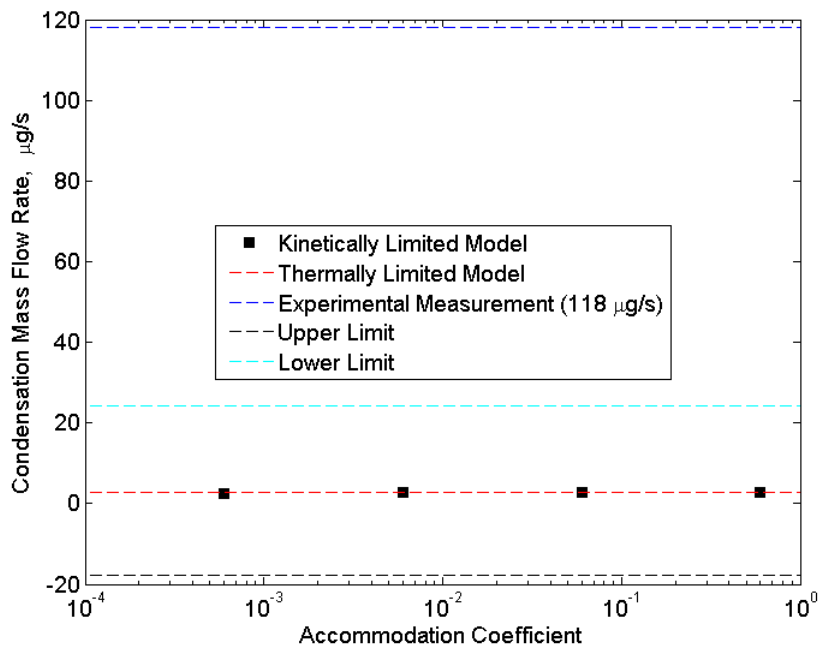
Figure 4.12. Condensation rate predictions using the different phase change models along with predictions for upper and lower limit of temperature measurement uncertainty. Experimental measurement is $118\,\mu g/s$.

Looking at the condensation rates presented in Figure 4.12, there are similarities with the evaporation rate predictions previously discussed. Similar to previous results, the condensation rate does not change with change in accommodation coefficient and the rate predicted by the kinetic model is identical to the predictions of the

thermal model. Although, the models do predict condensation at the liquid-vapor interface, the condensation rates predicted by these models using the exact temperature measurements are a few orders of magnitude smaller than the experimental measurement.

Looking at the temperature measurements from the temperature sensors used to formulate the boundary conditions, it can be seen that the temperatures on the side wall are all greater than the saturation temperature of $21\,K$ corresponding to a vapor pressure of $121.4\,kPa$ for hydrogen. This would explain the fact that the phase change at the liquid-vapor interface is a lot more evaporation dominated than expected to be. It is only the stick sensor on top of the test cell which would indicate any condensation at the liquid-vapor interface.

Table 4.5. Side wall temperatures measured by the temperature sensors used for boundary conditions in the computational model. Saturation temperature at $121.4\,kPa = 21\,K$, Volume $= 0.814\,cm^3$.

Sensor	Temperature (K)
S1	19.971
S2	21.012
S3	21.003
S4	21.798
Stick	20.718

In these calculations the offset in temperature sensor S4 is not accounted for. But, even with the $0.5\,K$ offset the temperature measured by sensor S4 would still be above the saturation temperature. One possible reason for this could be to do with the accuracy of the temperature sensors that are being used in the experiment. The side wall temperature sensors all have an uncertainty of $\pm0.25\,K$ and this would make the difference between the phase change being condensation dominated or evaporation

dominated. Formulating the boundary conditions by using the temperatures at the lower limit of uncertainty could have a significant effect on the phase change rate.

The phase change rates for both the upper and lower limit are shown in Figure 4.12. Negative values for the condensation rate represent evaporation at the liquid-vapor interface. This is expected at the upper limit based on the temperature measurements. Looking at the condensation rate predicted when both the temperature boundaries are set to the lower point of uncertainty, the numbers are much better. Although, the condensation rate predictions are significantly improved, they are still quite a bit away from the experimental values.

But looking closer at the experimental images, it was concluded that there are other considerations which affect the condensation calculations. It was noted that there was quite a bit of condensation in the thin film region and along the circular edge where the test cell and the lid meet at the top. This condensed liquid would then flow down the walls, contributing to the condensation rate. This makes sense as the interface is a zero degree contact angle interface which could have a very thin film all the way to the top of the test cell. As the condensation rate is calculated from the neutron imaging based on the change in liquid volume, it would be difficult to isolate just the condensation at the liquid-vapor interface. With such limitations in the condensation calculations, only computations for evaporation are studied in further detail in the chapters going forward.

5. EFFECT OF MEASUREMENT UNCERTAINTIES AND THIN FILM CONTRIBUTION ON PHASE CHANGE CALCULATIONS

As outlined in the previous chapter, the evaporation rates predicted by both the thermally limited and kinetically limited models are quite far from the experimental measurements. In this chapter, we look to bridge this gap between the two to better understand the problems with computational modeling of such phase change experiments and to help design better experiments in the future.

5.1 Thin-Film Contribution

In order to help with grid independence, the liquid-vapor interface was truncated below a thickness of 10 microns near the contact line. But based on the velocity distribution along the interface derived from the phase change rates, as shown in Figure 4.7, it is evident that the phase change contribution from this thin-film region would not be negligible. Cutting off the interface at a thickness of 10 microns in order to achieve grid independence reduces the interface area by about 5%. The phase change contribution from this missing region needs to be included for accurate phase change rate predictions. Instead of explicitly computing the phase change in the thin-film region, the phase change contribution is approximated using a rudimentary sub-grid scale model. The thin-film region is approximated as the surface of a truncated cone. The surface area and the midpoint of this surface can be found based on the available interface coordinates. Using the velocity computed along the known interface, the velocity at the midpoint of the missing region is extrapolated using a piece-wise linear fit. Higher order curve fits might help improve the velocity estimation

in the missing region but are not explored in this study as we only wanted to get an estimate for the contribution from the thin-film region.

Using an average density, the extrapolated velocity, and the surface area of the thin-film region, the phase change contribution from this region is estimated. The phase change from the small flat portion near the contact line shown in Figure 4.8 is subtracted from the computed total phase change rate. Based on these approximations, it is found that the thin-film region contributes to nearly 57% of the total evaporation rate. This means that there is an equal contribution to phase change from the bulk interface computed here and the missing thin-film region. Including this thin-film contribution in the evaporation rates predicted doubles the computationally predicted phase change rate. This brings the computational predictions much closer to the experimentally measured evaporation rate as shown in Figure 5.1. Using a better thin-film model such as the one proposed by Bellur [47] could help create a better estimate for the thin-film region.
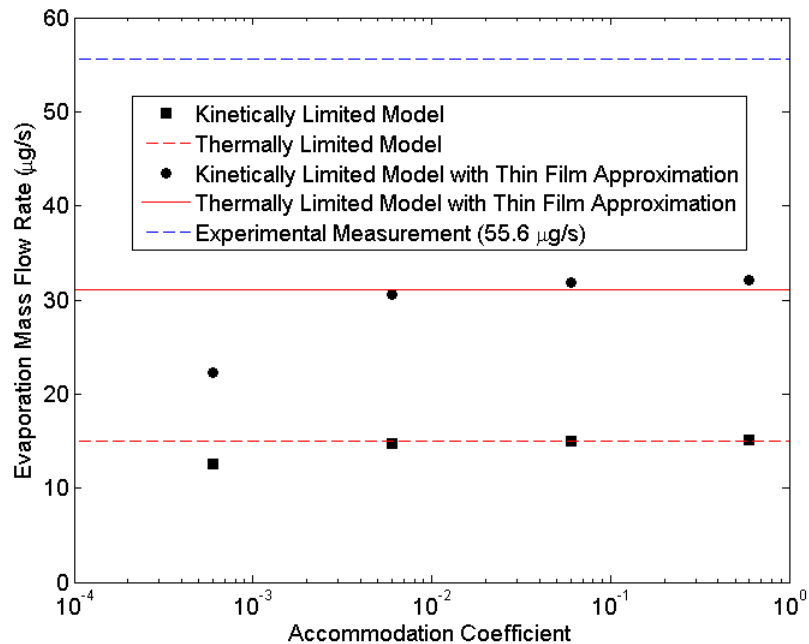

Figure 5.1. Effect of accommodation coefficient on evaporation rate predictions with and without thin-film approximation.

In order to further bridge the disparity between the computational predictions and the experimental data, the uncertainty in the temperature measurements are evaluated. The temperature sensors on the side wall of the test cell have an uncertainty of $\pm 0.25K$, whereas the sensor on top has an uncertainty of $\pm 1K$. Formulating the boundary conditions using the upper limit of uncertainty of these temperature measurements should help us understand the effect of this uncertainty. Only data at the upper limit is presented here because that would be the most relevant for this part. The effect of the temperature measurement uncertainty is discussed in further detail later in this chapter.
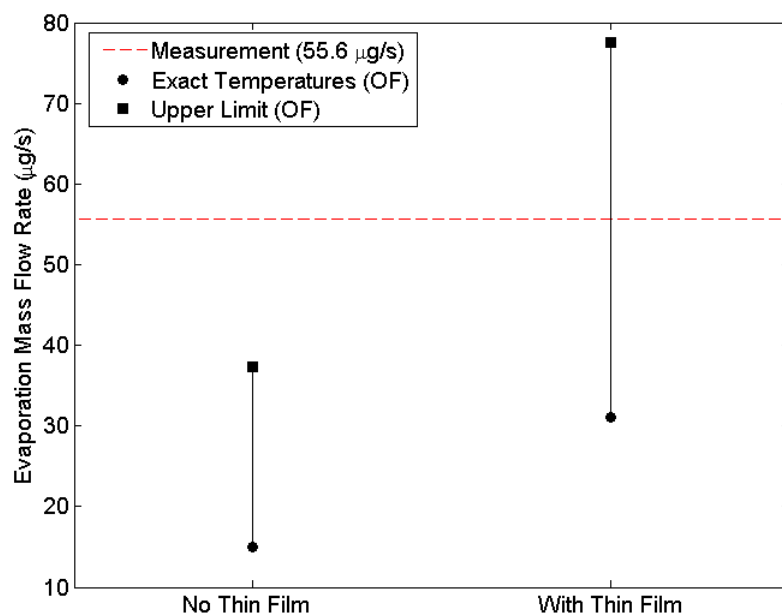
Figure 5.2. Effect of temperature sensor uncertainty on evaporation rate predictions showing effect of thin-film region. OF indicates Open-FOAM.

The evaporation rate estimated at the upper limit of uncertainty is nearly twice the prediction using the exact temperature measurements. When coupled with the thin-film approximation, the evaporation rate predicted at the upper limit of uncertainty shown in Figure 5.2 exceeds the experimental measurement. Hence, in some

(a)

(b)

Figure 5.3.   Comparison of saturation curves between Clausius-Clapeyron equation and NIST data for (a) $P_{ref} = 101.3\,kPa$ (b) $P_{ref} = 121\,kPa$.

Table 5.1. Evaporation rates predicted using the thermally limited phase change model for the two reference pressures considered.

Reference Pressure (kPa)	Computed Saturation Temperature (K)	Evaporation Rate ($\mu g/s$)
101.3	21.08	19.61
121	21	31.13

tions. As discussed previously, the temperatures on the side wall are measured using Lakeshore DT-670 temperature diodes which have an uncertainty of $\pm 0.25\,K$ while the temperature sensor on top of the lid has an uncertainty of $\pm 1\,K$. The temperature measurements for the evaporation calculations are presented in Figure 5.4 along with error bars indicating the uncertainty in these measurements.
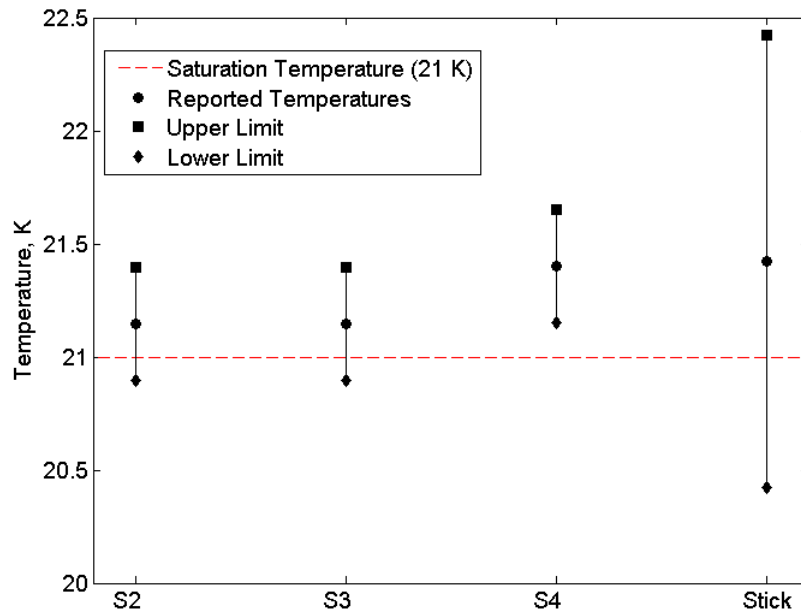
Figure 5.4. Temperature measurements from the four temperature sensors used for formulating boundary conditions with error bars indicating extremes of uncertainty.

In comparison to the saturation conditions, it is evident that at the lower limit of uncertainty, the temperature measurements from three of the temperature sensors are below the anticipated saturation temperature corresponding to the vapor pressure in the cell. This would indicate that the phase change at the liquid-vapor interface would be condensation dominated. The conditions in the experiment are close to saturation as evidenced by the low evaporation rates measured. In such conditions, even the smallest uncertainty in these temperature and pressure measurements would have a significant effect on the computational predictions for phase change rates. By setting the temperature boundary conditions at the extreme limits of the temperature sensor accuracy while keeping the pressure constant, the effect of temperature measurement uncertainty on evaporation can be quantified.

Since the phase change rates predicted by the kinetic model are unaffected by any change to the accommodation coefficient and are near identical to the rates predicted by the thermally limited model, the thermally limited model is used in the computations going forward to model phase change. This choice removes the uncertainty around the value of the accommodation coefficient as accurate values of accommodation coefficient are unavailable for hydrogen.

The thin film contribution is included in these computations as outlined in the previous section. The corresponding evaporation rates are presented in Figure 5.5. It is evident that at the upper limit of the temperature sensor uncertainty, the evaporation rate predicted is almost 2.5 times the prediction using reported temperature measurements. This comfortably pushes the computationally predicted evaporation rate over the reported experimental measurement. At the lower limit of the temperature measurement uncertainty, the phase change calculations show condensation at the liquid-vapor interface. This is expected as the temperature values at the lower limit of uncertainty are below the saturation temperature as discussed previously. Hence, based on the uncertainty in the temperature measurements, the phase change predicted could span anywhere from condensation to strong evaporation at the liquid-vapor interface.
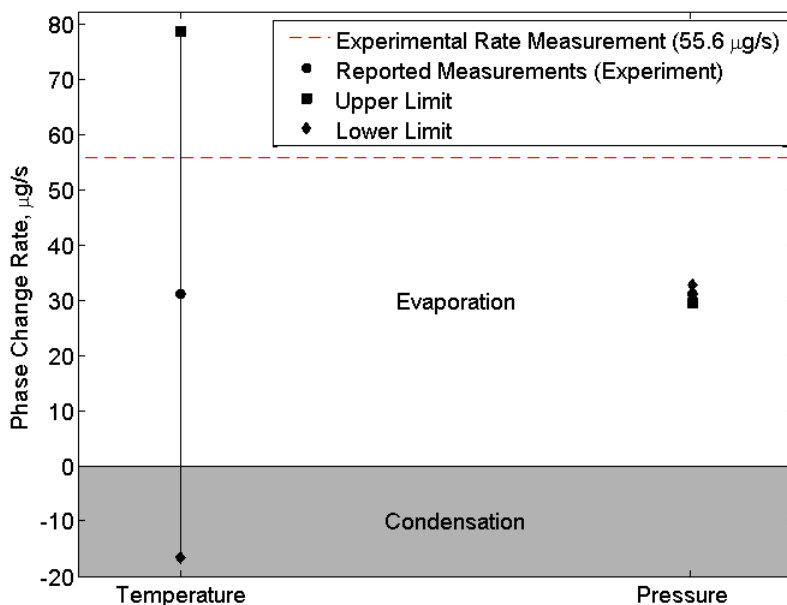
Figure 5.5. Phase change rate calculations at extremes of temperature and pressure sensor accuracy. Negative values indicate condensation at the liquid-vapor interface.

Similar to the temperature measurements, there is an uncertainty associated with the pressure measurements as well. The pressure is controlled by a throttling mechanism in the experiment which causes some degree of fluctuation in the pressure of the vapor maintained in the test cell. But the pressure measurements reported have an uncertainty which would have an effect on the evaporation rate calculations. The amount of uncertainty for the pressure transducer was unknown at the operating pressure levels. The pressure transducer was characterized for uncertainty at NIST while the experiment was conducted and was found to have an uncertainty of ±0.2%. Setting the pressure boundary condition at the extremes of this uncertainty should help quantify its effect on phase change calculations.

The corresponding evaporation rate predictions are presented in Figure 5.5. Although the evaporation rates are affected by the uncertainty in the pressure measurements, the effect is significantly smaller than the effect of temperature measurement

uncertainty. In the case of the pressure measurement uncertainty, the computational model predicts evaporation at both the upper and lower limits of uncertainty. Additionally, the change in evaporation rate is only $\pm 5\%$ in these calculations within the limits of the pressure sensor uncertainty.

Based on the computations for quantifying the effect of temperature and pressure uncertainties, it is quite clear that even small uncertainties in these measurements would have a significant effect on phase change calculations in the case of cryogenic systems in near equilibrium conditions. The kinetically limited phase change model is derived to work well in near equilibrium conditions owing to the assumptions inherent in the model. In full-scale tanks it is expected that at the liquid-vapor interface the conditions are close to saturation conditions. This is evidenced by the really small evaporation rates at the interface in the computations based on the k-site tank experiments [28]. Under such conditions, the phase change in these tanks is expected to be a thermally limited process and the accommodation coefficient would have a negligible effect on the phase change rates predicted. In near equilibrium calculations, the geometry of the liquid film would be a more important factor and accurate calculation of the phase change coming from the different liquid film regions would be much more important than the value of the accommodation coefficient.

When designing experiments to evaluate the kinetically limited phase change model, it is important to measure the temperatures and pressures in the system with reasonable accuracy. By addressing the uncertainties in these measurements, we should be able to get computational predictions much closer to the experimentally measured rates and reduce the uncertainty in the phase change rate predicted. Specific values for the accommodation coefficient of cryogenic propellants might exist in the kinetic regime of phase change. Experiments designed to study such phase change in the kinetic regime should address the uncertainties associated with the measurements. Otherwise, it would be difficult to computationally capture the thermal state of the experiment accurately and would produce large uncertainties in the value of the accommodation coefficient estimated.

In addition to the uncertainties discussed in this chapter, there are other factors (both computational and experimental) which could affect phase change predictions. There is a degree of uncertainty inherent in the liquid volume estimations and experimental phase change rates due to the image processing techniques used. The Hertz-Knudsen-Schrage equation in its initial form was derived for a flat planar interface, whereas here, it is being applied to an axisymmetric interface for a perfectly wetting fluid. Versions of the Hertz-Knudsen-Schrage model that include correction terms for the effect of interface curvature do exist and could be an important consideration while modeling regions with high interface curvature. One such model was proposed by Wayner [50] which under thermal equilibrium gives the following expression for the evaporation flux for a curved interface.

$$\dot{m} = \left(\frac{2\alpha}{2-\alpha}\right)\sqrt{\frac{M_v}{2\pi RT_i}}\left[\frac{p_v M_v L_b}{RT_v T_i}(T_i - T_v) - \frac{v_l p_v}{RT_i}(\Pi + \sigma\kappa)\right] \tag{5.1}$$

where Π is the disjoining pressure, σ is the surface tension, κ is the interface curvature, and v_l is the molar volume of the liquid. Average values for the interface temperature $(21\,K)$, vapor temperature $(21.06\,K)$, and interface curvature $(400\,1/m)$ are obtained from the computations. A simple calculation to compare the relative magnitudes of the different terms in Wayner's model using the ratio shown in Eq. 5.2 indicate that the curvature term is approximately four orders of magnitude smaller than the temperature difference term for these computations.

$$\Sigma = \frac{\rho_l L_b (T_i - T_v)}{\sigma\kappa T_v} \tag{5.2}$$

For the computations in this thesis, a quadratic function is used for the temperature boundary condition for the side wall as we are limited to measurements from only three temperature sensors. Using a higher order fit might improve the phase change computations. The liquid is treated as an incompressible fluid with no property variations in this computational model. Using a multiphase solver could help account for property variations in the liquid phase as well as relax the fixed interface assumption required in the case of this current solver. There are also unknown uncertainties as-

sociated with some of the fluid and solid properties used in these calculations from the NIST database. In the experiment, the pressure vent was asymmetric while in the computations the pressure vent was modeled as an axisymmetric vent. This could potentially affect the heat transfer to the interface through the solid regions. Additionally, estimating the thin-film contribution by extrapolating the velocity is a rudimentary subgrid model. Using a more robust subgrid model should improve the phase change predicted from the thin-film region. The extent to which such additional factors affect such phase change calculations remains to be seen and would be a good thing to investigate in further detail. However, in the case of this experiment, the uncertainty in the temperature measurements might still dominate these calculations. Any experiment designed in the future for the purpose of extracting accommodation coefficients need to be designed with these uncertainties in mind.

5.4 New Experiment Design with Varying Curvature for Phase Change Studies

Considering the success found by Bellur et al. [46] with imaging cryogens using neutron imaging, a slightly modified experimental setup is proposed to help alleviate some of the uncertainties discussed in previous chapters. In the experiments performed at NIST, a conical test cell was evaluated in order to try to maintain a planar interface for phase change. However since the cryogens used were perfectly wetting, the $10°$ cone was not very successful. As highlighted in previous chapters, the kinetic phase change model based on the Hertz-Knudsen-Schrage equation was originally derived for a flat planar interface. An experiment designed to measure phase change rates for a flat interface which would also be capable of producing interfaces with varying curvature would be vital to evaluate the effect of interface curvature on these models. This flat planar interface would remove the thin-film region close to the contact line seen in the original experiment.

The proposed test cell design with the solid regions of the test cell and the lid simplified as a single piece is considered here. The dimensions of this new test cell are kept similar to the one used in the NIST experiments as they are limited by the size of the cryostat and other components. The sharp edge helps to pin the contact line at that location. This would help obtain a series of interfaces with different interface curvatures varying from a perfectly wetted case to a flat interface as shown in Figure 5.6. This is important to study the effect of interface curvature on the kinetic phase change model.

(a)   (b)   (c)
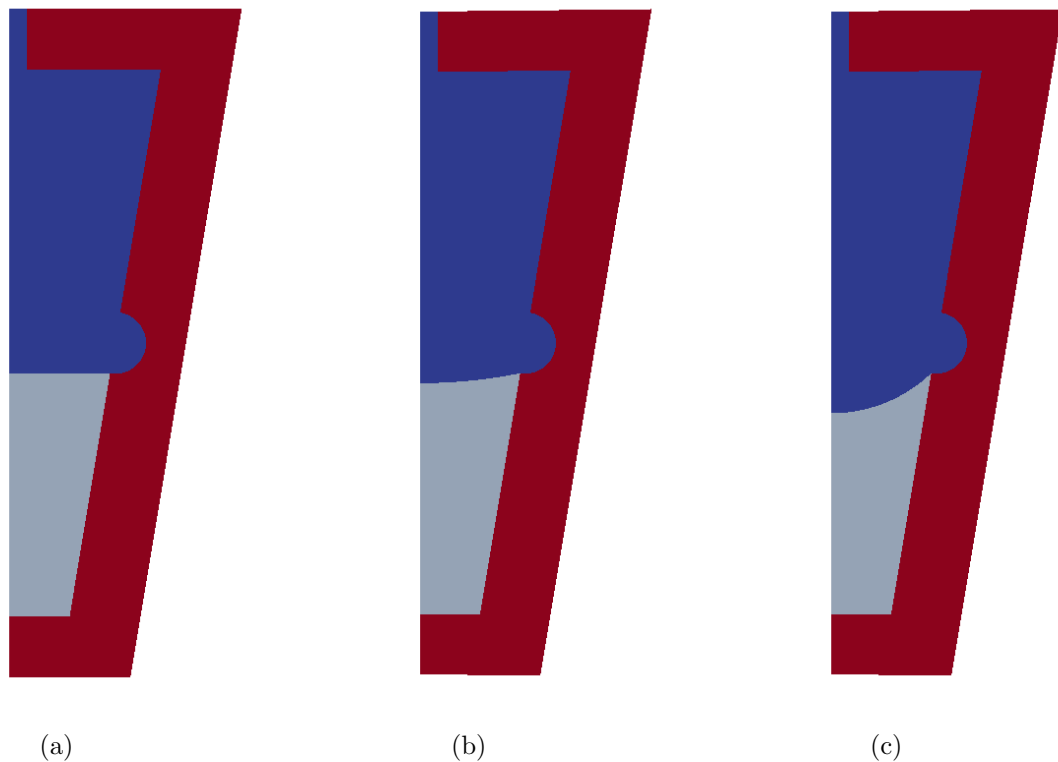
Figure 5.6. New experiment design to study accommodation coefficient. Three cases considered here (a) Case 1 - Flat interface (b) Case 2 - Curved interface with small interface curvature (c) Case 3 - Curved interface with large interface curvature. Dark Blue - Gas, Light Blue - Liquid, Red - Wall.

The test cell is treated as an axisymmetric model as in the original case. The pressure vent is retained as before as without it the pressure in the test cell would

increase and affect the saturation conditions. The test cell and the lid are combined here as the aim here is to get some preliminary data to test the viability of such an experiment. The vapor pressure in the test cell is set to $121.4\,kPa$ to be similar to the original experiment. This corresponds to a saturation temperature of $21\,K$. The outer boundary of the side wall was set as a constant temperature boundary with $21.2\,K$ in order to induce evaporation at the liquid-vapor interface. In these calculations, only side wall heating is considered and all other external walls are considered to be adiabatic. However for the experiment, temperature data along the outside wall of the test cell would enable more accurate boundary conditions for determining the thermal state of the test cell. It is important in the experiment to ensure that high accuracy temperature sensors are used and larger number of sensors are used to improve the accuracy of the boundary condition fits for the computational model and reduce the uncertainty in the phase change rates computed.

Computations were run for three different interface curvatures representative of the different states from a perfectly wetting interface to a flat interface. These interfaces all have constant curvature which would not be the case in reality. Using a solver which includes interface tracking such as a VOF method would help capture the dynamics of the pinned interface. The computations presented here were run with the kinetically limited phase change model with an accommodation coefficient value of 0.6. This is just an arbitrary value picked for these computations based on the data presented in previous chapters.

From the evaporation rate data presented in Figure 5.7, it is seen that both in the case of a flat interface and an interface with a small curvature we see an improvement in the phase change rate predicted with increasing grid resolution. As seen in the case of the perfectly wetting interface, the phase change represented by the interface velocity increases closer to the contact line as shown in Figure 5.8. In the previous section this was attributed to the thin film region of the interface, but based on the behaviour in the case of a flat interface, it can be concluded that this increase can occur in the case of any interface close to the contact line. This is potentially due to
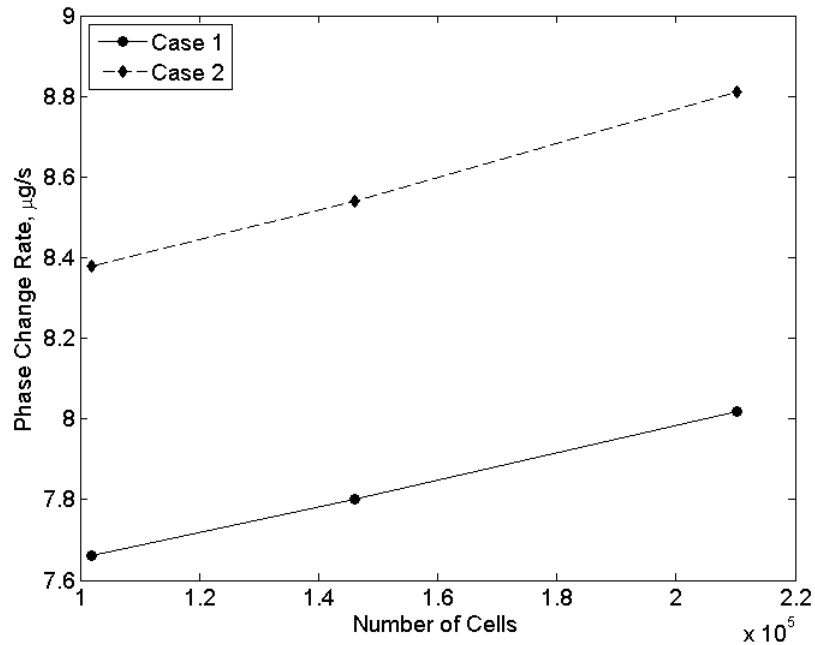
Figure 5.7. Evaporation rates computed using the kinetically limited
phase change model showing grid dependence for Case 1 and Case 2.

the higher temperature close to the contact line due to the solid wall. The CFD grids
used in these computations are unable to accurately capture the extremely small local
thermodynamics at the contact line, and this prevents an accurate prediction for the
evaporation rate. This problem explains the grid dependence issue in the case of both
the original experiment and the modified setup discussed here.

However, the relative contribution from this contact line region can be expected to
reduce drastically as the scale of the experiments are increased. When the experiments
become larger as in the case of a propellant tank, the circumference (representative
of the contact line) is proportional to the length while the area (representative of
the bulk interface) is proportional to the square of the length dimension. In the case
of the $10\,mm$ diameter test cell, the phase change contribution from the thin-film
region and the bulk interface are nearly equal. The LH2 tank at the Multi Hydrogen
Test Bed Facility was significantly larger with a tank diameter of $3.05\,m$. As the
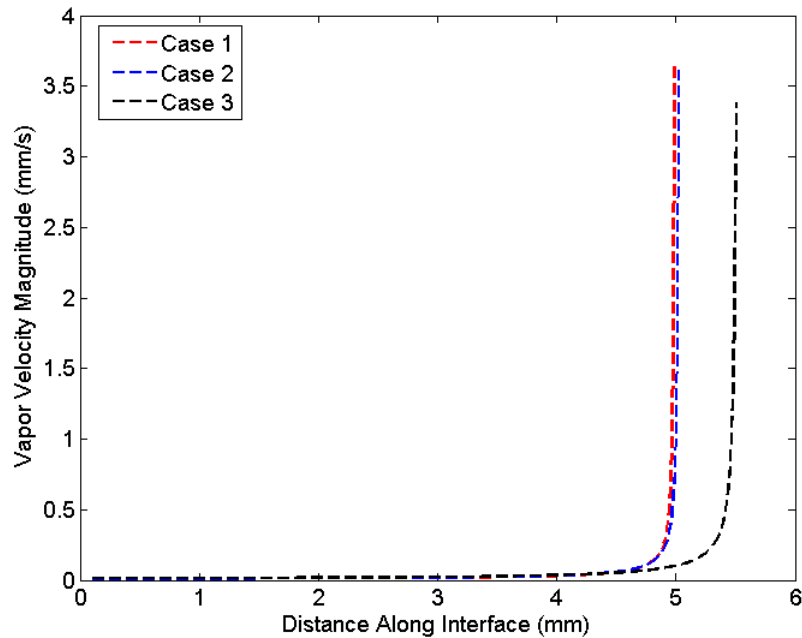
Figure 5.8. Velocity distribution along the interface showing a spike near the contact line for all the three cases considered.

experiments become larger the phase change is expected to be strictly dependent on the interface area. If the ratio of the phase change contribution from the thin-film region and the bulk interface scales inversely with the tank diameter, then in the case of the MHTB LH2 tank, the thin-film contribution can be expected to be less than a percentage of the total phase change rate. Hence for larger experiments, the phase change predictions would become much more accurate as there is less need to account for the contribution from the contact line region separately.

Looking at the evaporation rates for the three cases discussed here, it is seen that the evaporation rate increases with increases in interface curvature. This is the increase in phase change due to the increase in interface area which comes from the increase in curvature of the interface. Any additional effects of curvature are not included in these calculations and would need an alternate solver such as a VOF solver

Table 5.2. Evaporation rates predicted using the kinetically limited phase change model for the three cases considered.

Case #	Interface Area (mm^2)	Evaporation Rate ($\mu g/s$)
1	78.440	7.80
2	79.225	8.54
3	90.225	12.60

and using kinetic models such as Wayner's model which account for the contribution from interface curvature.

The data presented here shows the importance of addressing the local thermodynamics near the contact line for the computational model. One way to do this would be to insulate the wall near the contact line to prevent the wall temperature close to the contact line from being too high. This could be easy to implement in the experiment design presented here as the location of the contact line once it is pinned is known. An alternate way to solve this contact line problem would be to avoid the liquid to be in contact with the wall in the experiment design. Using a large suspended liquid droplet with phase change induced by controlling the temperature of the surrounding vapor would prevent the problems highlighted here with the contact line. For any experiment designed to study phase change in such cryogenic propellants, these are some additional considerations to ensure that the computational model adequately captures the thermodynamics and the thermal state of the experiment.

6. CONCLUSIONS

6.1 Summary

Proper storage and management of cryogenic propellants is going to be vital to long duration human space exploration. One problem plaguing such systems is the self-pressurization and pressure control of the propellant tanks. Estimating this pressurization and designing systems to manage this excess pressure is reliant on accurate phase change modeling as it would be nearly impossible to experimentally characterize each one of these systems. The kinetic phase change model governed by the Hertz-Knudsen-Schrage equation is the model of choice for such phase change computations. Critical to the model is the accommodation coefficient which accounts for the non-continuum effects associated with phase change. The focus of the research undertaken was to study some of the uncertainties associated with the accommodation coefficient and to decipher values for the accommodation coefficient in the case of cryogens. This would enable improved phase change modeling in the case of cryogenic propellant systems.

To extract these accommodation coefficients there is a need for hybrid experimental and computational studies specifically built for this purpose. A few experiment designs with the aim to study the different uncertainties associated with phase change modeling were analyzed using CFD calculations. Both the thermally limited and the kinetically limited phase change model were implemented within the conjugate heat transfer solver in OpenFOAM. The implementation of the Hertz-Knudsen-Schrage equation using an iteration method by coupling it with an interfacial energy balance was also discussed. This was found to be the most accurate method of implementing the model in comparison to the averaging or the interpolation techniques that were considered. A sample benchmark case representative of the test section in one of

the experiment designs was set up to obtain initial trends using the different phase change models implemented.

A computational model of the phase change experiment for a liquid hydrogen meniscus evaporating and condensing within a cylindrical aluminum vessel was used to evaluate the two phase change models. Since cryogens are perfectly wetting fluids, modeling the zero degree contact angle interface led to a grid dependence problem due to its multiscale nature. The velocity along the interface indicated that there was a spike in the local phase change near the contact line. Increasing the grid resolution improved the prediction of this peak velocity. In order to ensure grid independence, a small portion of the interface below $10\,\mu m$ was cut off near the contact line.

6.2   Conclusions

The evaporation rate predicted by both the thermally limited and the kinetically limited phase change models were found to be similar. In the case of the kinetically limited phase change model, it was seen that the phase change rates were insensitive to any change to the value of the accommodation coefficient for about three orders of magnitude. This trend was also noticed in the case of the benchmark case. In the benchmark case, it was seen that the interface temperature (and consequently the interface pressure difference) adjusted itself to account for the change in accommodation coefficient. This could be attributed to the fact that in near equilibrium conditions, the phase change is thermally limited as shown by the near identical rates predicted by the two models. This could also potentially explain the three order of magnitude scatter that is seen in the reported value of the accommodation coefficient for any given fluid. The predicted evaporation rates were found to be much lesser than the experimentally measured evaporation rate.

The thin-film region close to the contact line and below a film thickness of $10\,\mu m$ was found to contribute to about 57% of the total mass flow rate predicted, even though it accounts for only 5% of the total interface area. The effects of the tempera-

ture and pressure measurement uncertainties on phase change were also evaluated. It was found that the effect of temperature measurement uncertainty was significantly higher than the effect of the pressure measurement uncertainty. The pressure uncertainty caused only a $\pm 5\%$ change in the predicted evaporation rate. The temperature measurement uncertainty calculations on the other hand predicted condensation at the lower limit of uncertainty and improved evaporation at the upper limit of uncertainty. Hence the uncertainty on these measurements produces a wide range of uncertainty in the phase change rate predicted. It was also shown that in some combination these uncertainties can help bridge the gap between the experimental measurements and the computational predictions.

The phase change predictions were also found to be dependent on the reference pressure used in the Clausius-Clapeyron equation for estimating the saturation conditions. Additional sources of uncertainty both from the experiment and the computational model were also discussed. The Hertz-Knudsen-Schrage equation for instance was derived for a planar flat interface for near equilibrium conditions. In the computations presented here the model was applied to an axisymmetric perfectly wetting interface. Using high resolution temperature and pressure sensors along with finer pressure control systems should reduce some of the uncertainties in the experiments and help future experiments designed to better extract accommodation coefficient.

6.3 Recommendations for Future Research

The independence of the phase change predictions on the value of the accommodation coefficient shows that at near equilibrium conditions, other factors such as the liquid distribution inside of the tank would have a bigger impact on phase change predictions. The tank experiments studied thus far indicate that they operate in near equilibrium conditions where the phase change would be a thermally limited process. Experiments designed to operate in the kinetic regime of phase change could help extract specific values for the accommodation coefficient.

A modified experimental setup to study phase change for a planar interface was proposed with the aim of removing the uncertainty associated with the thin-film region close to the contact line. Such an experiment would also be capable of producing interfaces with different curvatures. Based on some initial calculations for such a setup, it was seen that having a flat planar interface does not solve the grid dependence problem seen in the original experiment. This is attributed to the high heat flux from the solid wall close to the contact line and the inability of the current CFD calculations to accurately model the small local thermodynamics at the contact line.

Experiments designed in the future to extract accommodation coefficients need to address the issues outlined in this section. Larger experiments might help reduce the contribution from the thin film region but add additional physics to account for such as buoyancy driven fluid convection. As the experiments become larger, the phase change predictions would become strictly dependent on the interface area. Alternatively, the contact line region can be managed by insulating a portion of the wall close to the contact line. This helps to control the heat flux going into the liquid at the contact line. Additionally, the uncertainties in the temperature and pressure measurements need to be reduced by using more accurate sensors. Having more sensors would also help improve the accuracy of the boundary conditions used in the computational model.

On the computational side, using a conjugate heat transfer solver capable of solving multiphase flow using the VOF method would help circumvent some of the issues with interface curvature and can help capture the dynamics of the interface movement with phase change. In the case of any phase change experiment in a closed container a pressure vent is necessary, as the pressure of the vapor and as a consequence the saturation conditions would continuously vary otherwise. However, it is important to reconsider the location of the pressure vent to make it easier to incorporate in the computational model.

REFERENCES

[1] NASA Architecture Steering Group and Bret G. Drake. *Human Exploration of Mars Design Reference Architecture 5.0*, 2009. NASA/SP-2009-566.

[2] Susan Motil, Michael Meyer, and Stephen Tucker. Cryogenic Fluid Management Technologies for Advanced Green Propulsion Systems. In *45th AIAA Aerospace Sciences Meeting and Exhibit*, 2007. AIAA 2007-343.

[3] C.B. Muratov, Viatcheslav V. Osipov, and Vadim N. Smelyanskiy. Issues of Long-Term Cryogenic Propellant Storage in Microgravity. 2011. NASA/TM-2011-215988.

[4] David J. Chato. Low Gravity Issues of Deep Space Refueling. *43rd Aerospace Sciences Meeting and Exhibit*, 2005. AIAA 2005-1148.

[5] Mohammad Kassemi, Sonya Hylton, and Olga V. Kartuzova. Zero-Boil-Off Tank (ZBOT) Experiment - Ground-Based Validation of Two - Phase Self-Pressurization CFD Model & Preliminary Microgravity Results. In *2018 Joint Propulsion Conference*. American Institute of Aeronautics and Astronautics, 2018. AIAA 2018-4940.

[6] W. U. Notardonato, A. M. Swanger, J. E. Fesmire, K. M. Jumper, W. L. Johnson, and T. M. Tomsik. Zero Boil-Off Methods for Large-Scale Liquid Hydrogen Tanks Using Integrated Refrigeration and Storage. *IOP Conference Series: Materials Science and Engineering*, 278(1), 2017.

[7] Mohammad M. Hasan, Chin S. Lin, Richard H. Knoll, and Michael D. Bentz. Tank Pressure Control Experiment: Thermal Phenomena in Microgravity. 1996. NASA-TP-3564.

[8] John C. Aydelott. Normal Gravity Self-Pressurization of 9-inch-(23 cm) Diameter Spherical Liquid Hydrogen Tankage. 1967. NASA TN-D-4171.

[9] John C. Aydelott. Effect of Gravity on Self-Pressurization of Spherical Liquid-Hydrogen Tankage. 1967. NASA TN-D-4286.

[10] J.C. Aydelott and C.M. Spuckler. Effect of Size on Normal-Gravity Self-Pressurization of Spherical Liquid Hydrogen Tankage. 1969. NASA TN-D-5196.

[11] M.M. Hasan, C.S. Lin, and N.T. Vandresar. Self-Pressurization of a Flightweight Liquid Hydrogen Storage Tank Subjected to Low Heat Flux. 1991. NASA TM-103804.

[12] N.T. Van Dresar, C.S. Lin, and M.M. Hasan. Self-Pressurization of a Flightweight Liquid Hydrogen Tank - Effects of Fill Level at Low Wall Heat Flux. *30th Aerospace Sciences Meeting and Exhibit*, 1992. AIAA 1992-0818.

[13] Louis J. Poth and James R. Van Hook. Control of the Thermodynamic State of Space-Stored Cryogens by Jet Mixing. *Journal of Spacecraft and Rockets*, 9(5):332–336, 1972.

[14] C.S. Lin, M.M. Hasan, and N.T. Vandresar. Experimental Investigation of Jet-Induced Mixing of a Large Liquid Hydrogen Storage Tank. *6th Joint Thermophysics and Heat Transfer Conference*, 1994. AIAA 1994-2079.

[15] L.J. Hastings, R.H. Flachbart, J.J. Martin, A. Hedayat, M. Fazah, T. Lak, H. Nguyen, and J.W. Bailey. Spray Bar Zero-Gravity Vent System for On-Orbit Liquid Hydrogen Storage. 2003. NASA/TM-2003-212926.

[16] W.D. Ward, L.E. Toole, C.A. Ponder, M.E. Meadows, C.W. Simmons, J.H. Lytle, J.M. McDonald, and B.M. Kavanaugh. Evaluation of AS-203 Low-Gravity Orbital Experiment. 1967. NASA CR-94045.

[17] Stephen Barsi and Mohammad Kassemi. Investigation of Tank Pressurization and Pressure Control – Part I: Experimental Study. *Journal of Thermal Science and Engineering Applications*, 5(4):041005, 2013.

[18] K. Bellur, E.F. Médici, M. Kulshreshtha, V. Konduru, D. Tyrewala, A. Tamilarasan, J. McQuillen, J.B. Leão, D.S. Hussey, D.L. Jacobson, et al. A New Experiment for Investigating Evaporation and Condensation of Cryogenic Propellants. *Cryogenics*, 74:131–137, 2016.

[19] C.S. Lin and M.M. Hasan. Self-Pressurization of a Spherical Liquid Hydrogen Storage Tank in a Microgravity Environment. *30th Aerospace Sciences Meeting and Exhibit*, 1992. AIAA 1992-0363.

[20] John I. Hochstein, Philip M. Gerhart, and J.C. Aydelot. Computational Modeling of Jet Induced Mixing of Cryogenic Propellants in Low-g. *20th Joint Propulsion Conference*, 1984. AIAA 1984-1344.

[21] John I. Hochstein, Hyun-Chul Ji, and John C. Aydelott. Prediction of Self-Pressurization Rate of Cryogenic Propellant Tankage. *Journal of Propulsion and Power*, 6(1):11–17, 1990.

[22] Gary Grayson, Alfredo Lopez, Frank Chandler, Leon Hastings, and Stephen Tucker. Cryogenic Tank Modeling for the Saturn AS-203 Experiment. *42nd AIAA/ASME/SAE/ASEE Joint Propulsion Conference and Exhibit*, 2006. AIAA 2006-5258.

[23] Charles H. Panzarella and Mohammad Kassemi. On the Validity of Purely Thermodynamic Descriptions of Two-Phase Cryogenic Fluid Storage. *Journal of Fluid Mechanics*, 484:41–68, 2003.

[24] Charles H. Panzarella and Mohammad Kassemi. Self-Pressurization of Large Spherical Cryogenic Tanks in Space. *Journal of Spacecraft and Rockets*, 42(2):299–308, 2005.

[25] Charles H. Panzarella and Mohammad Kassemi. Comparison of Several Zero-Boil-Off Pressure Control Strategies for Cryogenic Fluid Storage in Microgravity. *Journal of Propulsion and Power*, 25(2):424–434, 2009.

[26] S. Barsi and M. Kassemi. Numerical and Experimental Comparisons of the Self-Pressurization Behavior of an LH2 Tank in Normal Gravity. *Cryogenics*, 48(3):122–129, 2008.

[27] Olga Kartuzova and Mohammad Kassemi. Modeling Interfacial Turbulent Heat Transfer During Ventless Pressurization of a Large Scale Cryogenic Storage Tank in Microgravity. *47th AIAA/ASME/SAE/ASEE Joint Propulsion Conference & Exhibit*, 2011. AIAA 2011-6037.

[28] Mohammad Kassemi and Olga Kartuzova. Effect of Interfacial Turbulence and Accommodation Coefficient on CFD Predictions of Pressurization and Pressure Control in Cryogenic Storage Tank. *Cryogenics*, 74:138 – 153, 2016.

[29] Mark Stewart and Jeffrey P. Moder. Self-Pressurization of a Flightweight, Liquid Hydrogen Tank: Simulation and Comparison with Experiments. *52nd AIAA/SAE/ASEE Joint Propulsion Conference*, 2016. AIAA 2016-4674.

[30] Mohammad Kassemi, Olga Kartuzova, and Sonya Hylton. Validation of Two-Phase CFD Models for Propellant Tank Self-Pressurization: Crossing Fluid Types, Scales, and Gravity Levels. *Cryogenics*, 89:1 – 15, 2018.

[31] H. Hertz. Ueber die Verdunstung der Flüssigkeiten, insbesondere des Quecksilbers, im luftleeren Raume. *Annalen der Physik*, 253(10):177–193, 1882.

[32] Martin Knudsen. Die maximale Verdampfungsgeschwindigkeit des Quecksilbers. *Annalen der Physik*, 352(13):697–708, 1915.

[33] Robert W. Schrage. *A Theoretical Study of Interphase Mass Transfer*. PhD thesis, Columbia University Press, 1953.

[34] R. Marek and J. Straub. Analysis of the Evaporation Coefficient and the Condensation Coefficient of Water. *International Journal of Heat and Mass Transfer*, 44(1):39–53, 2001.

[35] John Vieceli, Martina Roeselová, and Douglas J. Tobias. Accommodation Coefficients for Water Vapor at the Air/Water Interface. *Chemical Physics Letters*, 393(1):249–255, 2004.

[36] P. Davidovits, D. R. Worsnop, J. T. Jayne, C. E. Kolb, P. Winkler, A. Vrtala, P. E. Wagner, M. Kulmala, K. E. J. Lehtinen, T. Vesala, and M. Mozurkewich. Mass Accommodation Coefficient of Water Vapor on Liquid Water. *Geophysical Research Letters*, 31(22), 2004.

[37] Michael Mozurkewich. Aerosol Growth and the Condensation Coefficient for Water: A Review. *Aerosol Science and Technology*, 5(2):223–236, 1986.

[38] Sandra L. Lednovich and John B. Fenn. Absolute Evaporation Rates for Some Polar and Nonpolar Liquids. *AIChE Journal*, 23(4):454–459.

[39] Bing-Yang Cao, Jian-Fei Xie, and Sergei S. Sazhin. Molecular Dynamics Study on Evaporation and Condensation of n-dodecane at Liquid–Vapor Phase Equilibria. *The Journal of Chemical Physics*, 134(16):164309, 2011.

[40] B. Paul. Compilation of Evaporation Coefficients. *ARS Journal*, 32(9):1321–1328, 1962.

[41] Jonathan Barrett and Charles Clement. Kinetic Evaporation and Condensation Rates and their Coefficients. *Journal of Colloid and Interface Science*, 150(2):352 – 364, 1992.

[42] Masataka Okuyama and Joseph T. Zung. Evaporation–Condensation Coefficient for Small Droplets. *The Journal of Chemical Physics*, 46(5):1580–1585, 1967.

[43] Aaron H. Persad and Charles A. Ward. Expressions for the Evaporation and Condensation Coefficients in the Hertz-Knudsen Relation. *Chemical Reviews*, 116(14):7727–7767, 2016.

[44] E.J. Davis. A History and State-of-the-Art of Accommodation Coefficients. *Atmospheric Research*, 82(3):561–578, 2006.

[45] OpenFoam Foundation. OpenFOAM v2.3.0. `www.openfoam.org`, Version Released 17 Feb 2014.

[46] Kishan Bellur, Vinaykumar Konduru, Ezequiel F. Medici, Daniel S. Hussey, David L. Jacobson, Jacob M. LaManna, Jeffrey S. Allen, and Chang Kyoung Choi. Visualization of the Evaporation and Condensation Phenomena in Cryogenic Propellants. *Journal of Flow Visualization and Image Processing*, 23(1-2):137–156, 2016.

[47] Kishan Bellur. *A New Technique to Determine Accommodation Coefficients of Cryogenic Propellants*. PhD thesis, Michigan Technological University, 2018.

[48] William G. Lindsley, Steven H. Collicott, Gunter N. Franz, Brian Stolarik, Walter McKinney, and David G. Frazer. Asymmetric and Axisymmetric Constant Curvature Liquid-Gas Interfaces in Pulmonary Airways. *Annals of Biomedical Engineering*, 33(3):365–375, 2005.

[49] Peter E. Bradley and Ray Radebaugh. Properties of Selected Materials at Cryogenic Temperatures. In *CRC Handbook of Chemistry and Physics*. CRC Press, Boca Raton, FL, 2013.

[50] Peter C. Wayner. The Effect of Interfacial Mass Transport on Flow in Thin Liquid Films. *Colloids and Surfaces*, 52:71 – 84, 1991.

A. CFD ANALYSIS OF EXPERIMENT DESIGN

As part of the experiment design, a preliminary CFD analysis was performed to evaluate different ideas for producing a steady, repeatable, and controllable convective flow over a liquid droplet. A simple circular cylinder dewar with an active region (droplet) at the bottom center was considered initially for this purpose. Based on initial CFD results for a range of aspect ratios (L/D ratios) ranging from 0.5 to 3, it was found that such a set up would struggle to produce a steady controlled convective flow over the active region. Select results for L/D = 0.5 and 2 are shown in Figure A.1(a) and Figure A.1(b) respectively. In all these calculations, a portion of the lower wall was set at a constant external temperature of $80\,K$ to simulate condensation conditions near the base of the vessel. All other external walls were maintained at a constant temperature of $100\,K$.

In these computations, although a convection cell was generated, it was found that at the droplet location the velocity was unsteady and also produced a stagnation point above the droplet. The regions of reasonably uniform velocity were found to be along the base (for L/D = 0.5) and along the side walls (for L/D = 2) depending on the aspect ratio. There was also some asymmetry noticed in the positioning of these convection cells with some switching between different asymmetric configurations. Placing the droplet off the central axis in such a setup would remove some of the uncertainties in the velocity over the active region in comparison to the central placement but would still have some unsteady behavior.

Based on the data from these initial computations, the experiment design was updated to constraint the flow within a low speed cryogenic tunnel instead of attempting to form a free form convective cell. A convectively driven mini wind tunnel works on a similar principle to a thermosyphon.

70
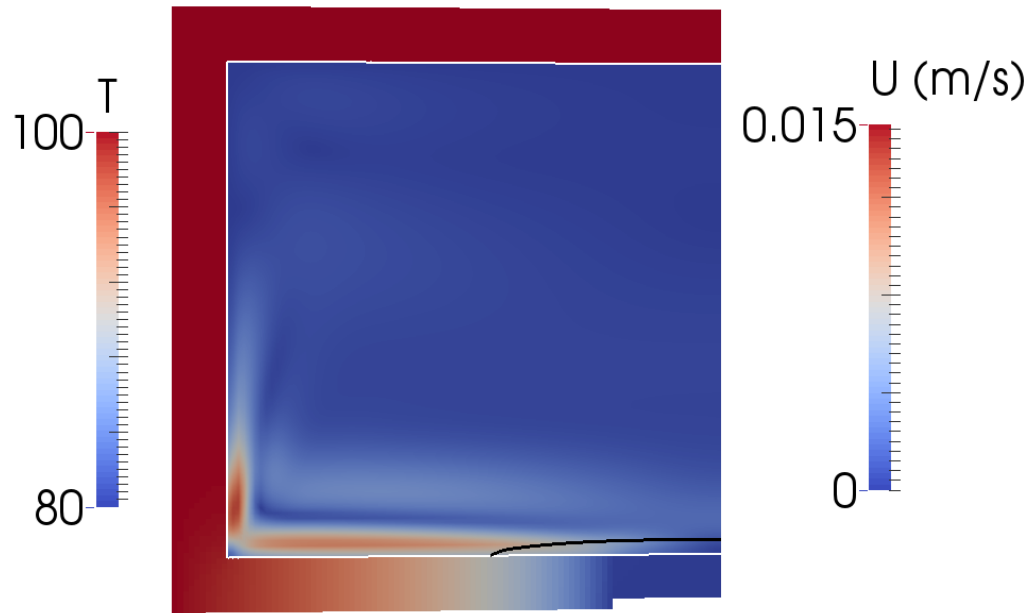
(a) L/D = 0.5
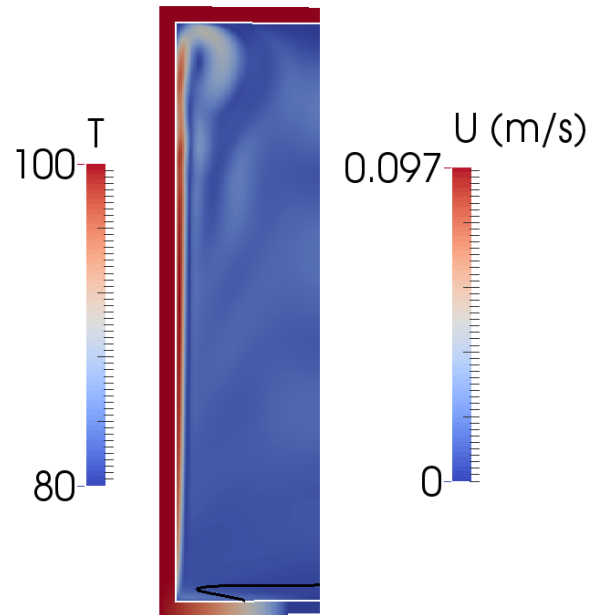
(b) L/D = 2.0

Figure A.1. Axisymmetric calculation for different L/D with black contour at $90\,K$. Right edge is the axis of rotation for the cylindrical domain. Contours indicate temperature of the dewar wall and velocity of the gas inside the cylinder.
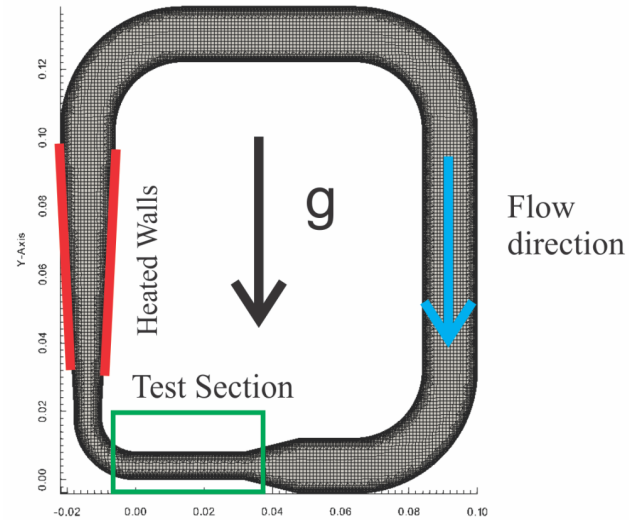
(a)
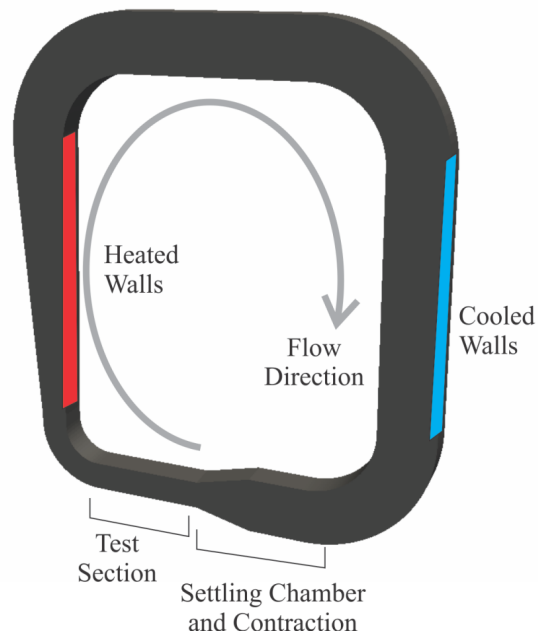
(b)

Figure A.2. Miniature convection driven cyrogenic tunnel which is to be placed inside the cryostat.

This wind tunnel is placed inside a cryostat to keep the system at the necessary temperatures. Flow is driven in the tunnel by heating the expanding vertical arm on

the left and cooling the other vertical arm to ensure that there is no net heat input into the system. The top and bottom sections of the tunnel are exposed to the bulk fluid in the cryostat which is maintained at around $100\,K$. The bottom arm of the tunnel is the test section which is where we require steady controlled vapor convection. The liquid droplet is formed at the active site within the test section through LN2 control of temperature at the base of a silver cup (active site). Evaporation or condensation is induced by controlling this temperature at the base of the silver cup. The entire tunnel is about $10\,cm$ x $10\,cm$ x $2\,cm$ in size.
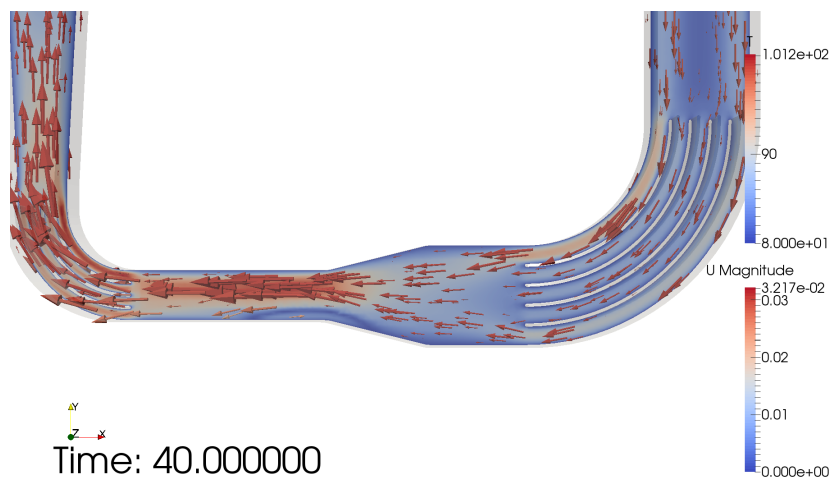

Figure A.3. Contours of velocity showing flow separation in the convergent section of the tunnel.

Looking at some early computations with a convergent section as initially proposed, some reverse flow was observed in the converging section of the tunnel. The ratio of hydrostatic to dynamic pressure at the entrance to the converging section was found to be quite a high number which essentially meant that due to the really small velocity in the test section flow separation could occur due to the denser fluid flowing down the slope of the converging section. To mitigate this, the bottom of the tunnel was flattened to have an elliptic converging section. To validate this new design, computations were run for two different heat flux values viz. $1\,W/m^2$ and $0.0625\,W/m^2$ in the expanding arm of the tunnel. An equivalent amount of heat was

removed from the other vertical arm of the tunnel. The two horizontal sections of the tunnel were assumed to have adiabatic external walls. The active site in the test section was assumed to be a solid wall at a fixed temperature for simplicity. The velocity contours at start up conditions for $1\,W/m^2$ of heating in the expanding arm and no additional heating or cooling at the active site is shown in Figure A.4.
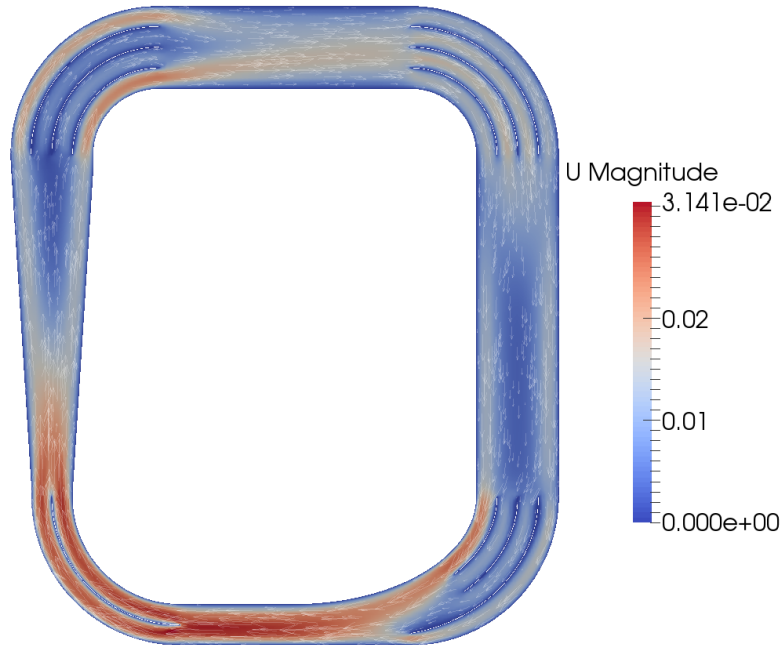

Figure A.4. Velocity contours at start up for the updated cryogenic tunnel loop. Heating of $1\,W/m^2$ on the vertical arm produces velocities of around $3\,cm/s$ in the test section.

The test section velocity is to be controlled by varying the input power into the heated expansion section of the tunnel. The temperature and velocity profiles entering the test section at $10\,s$ intervals are presented for the two heating powers in Figure A.5. For the higher heater power of $1\,W/m^2$ the flow in the test section is slightly unsteady but this can be rectified by adjusting the turning vanes before the flow enters the test section. The flow in the test section is from right to left, and is the

reason for the negative velocities in these plots. As the heater power is changed from $1\,W/m^2$ to $0.0625\,W/m^2$ the change in velocity is not too drastic.
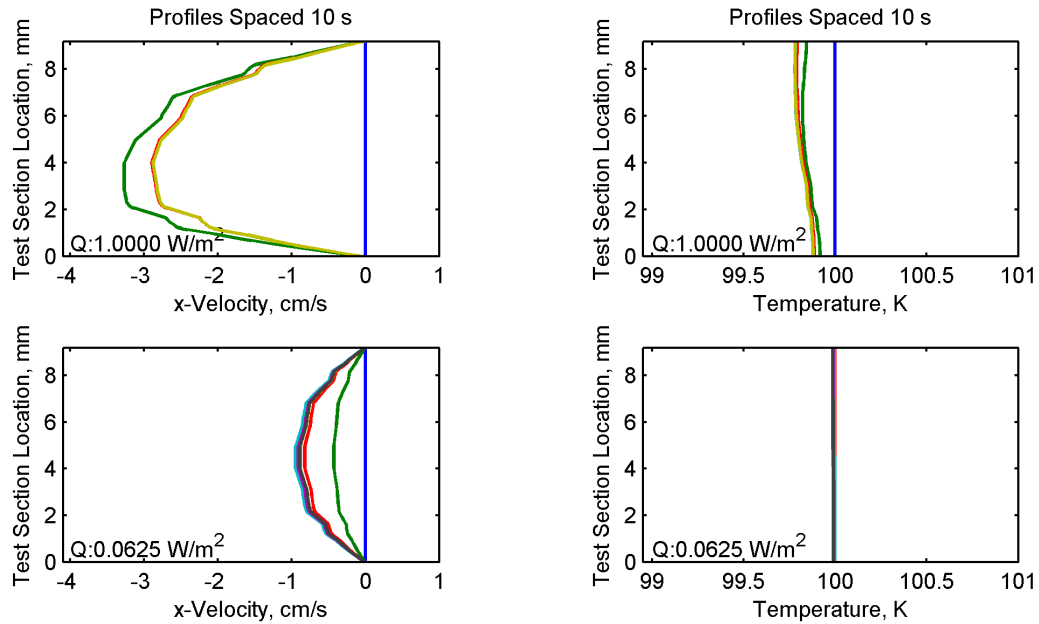

Figure A.5. Velocity (left) and Temperature (right) profiles at the test section inlet under start up conditions for both heater powers. Profiles are plotted at $10\,s$ intervals.

The temperature profiles for the higher heater power of $1\,W/m^2$ show a slight deviation from the bulk temperature but the reduction in heater power brings the temperature closer to $100\,K$. The expected convection velocity is around $1\,cm/s$ in real case scenarios which is quite easily achievable in this tunnel. A much lower heater power is sufficient to achieve this velocity and would help reduce any potential unsteady behavior and temperature deviations in the real experiment.
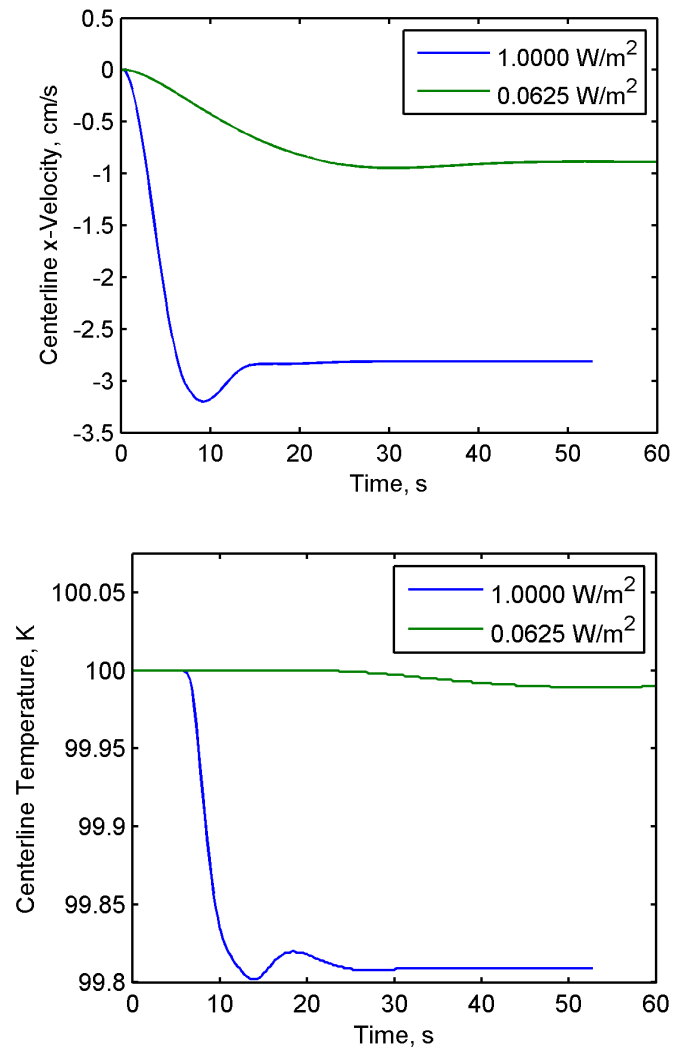
Figure A.6. Centerline velocity (top) and temperature (bottom) variation with time showing steady nature of the flow in the test section.